

## STRUCTURAL BIOLOGY

# Cryo-EM structure of PepT2 reveals structural basis for proton-coupled peptide and prodrug transport in mammals

Joanne L. Parker<sup>1\*†</sup>, Justin C. Deme<sup>2,3,4†</sup>, Zhiyi Wu<sup>1†</sup>, Gabriel Kuteyi<sup>1</sup>, Jiandong Huo<sup>5,6,7</sup>, Raymond J. Owens<sup>5,6,7</sup>, Philip C. Biggin<sup>1\*</sup>, Susan M. Lea<sup>2,3,4\*</sup>, Simon Newstead<sup>1,8\*</sup>

The SLC15 family of proton-coupled solute carriers PepT1 and PepT2 play a central role in human physiology as the principal route for acquiring and retaining dietary nitrogen. A remarkable feature of the SLC15 family is their extreme substrate promiscuity, which has enabled the targeting of these transporters for the improvement of oral bioavailability for several prodrug molecules. Although recent structural and biochemical studies on bacterial homologs have identified conserved sites of proton and peptide binding, the mechanism of peptide capture and ligand promiscuity remains unclear for mammalian family members. Here, we present the cryo-electron microscopy structure of the outward open conformation of the rat peptide transporter PepT2 in complex with an inhibitory nanobody. Our structure, combined with molecular dynamics simulations and biochemical and cell-based assays, establishes a framework for understanding peptide and prodrug recognition within this pharmaceutically important transporter family.

## INTRODUCTION

Solute carrier (SLC) transporters play essential roles in regulating small-molecule transport across biological membranes and are critical for cellular homeostasis. The SLC15 family of proton-coupled peptide transporters is the principal route through which animals absorb and retain dietary nitrogen (1). Whereas ingested protein is absorbed across the intestinal brush border membrane via the plasma membrane peptide transporter, PepT1 (SLC15A1) (2), circulating peptides are retained in the body through reabsorption in the kidneys, where PepT2 (SLC15A2) acts to selectively reuptake peptides from the glomerular filtrate (Fig. 1A) (3).

PepT2 is widely expressed in the human body, where, in addition to peptide retention in the kidney, the transporter also acts to regulate peptide transport across the blood-brain barrier in the choroid plexus (4). A remarkable feature of both PepT1 and PepT2 is their ability to recognize a diverse range of di- and tripeptide ligands (5), which results in these transporters playing an important role in drug transport, with well-known drug classes, including  $\beta$ -lactam antibiotics and several antiviral and anticancer drugs, being recognized and transported (6). PepT1 and PepT2 have been successfully targeted for the development of prodrugs, such as valacyclovir and valganciclovir, which exhibit improved oral bioavailability and retention in the human body through their ability to use PepT1 and PepT2 to cross the plasma membrane (7, 8). The location of PepT1

and PepT2 at sites of solute absorption makes these transporters excellent targets for improving drug uptake and retention in the human body (9). However, to date, structural information on the mammalian transporters is unavailable, hampering efforts to develop three-dimensional (3D) structural templates for peptide and drug recognition.

The SLC15 family form part of the proton-coupled oligopeptide transporter or POT family, members of which are widely distributed within pro- and eukaryotic genomes (10). POT family transporters belong to the major facilitator superfamily (MFS). They are all proton ( $H^+$ )-driven symporters using the inwardly direct proton electrochemical gradient ( $\Delta\mu H^+$ ) to drive the concentrative uptake of peptides across cell and organelle membranes (11). To date, a wide array of prokaryotic peptide transporters have successfully been used as model systems to study ligand recognition and transport within the POT family (12). However, despite numerous structures from different bacterial species, none have been captured in the outward-facing state, which is responsible for the initial capture of peptides and drugs from the extracellular side of the membrane. The bacterial structures have also been unable to inform on the structural relationship between the transporter and a large extracellular domain (ECD) unique to PepT1 and PepT2 and that is proposed to localize trypsin to the site of peptide transport (13).

To address these outstanding questions, we determined the structure of the mammalian PepT2 transporter from *Rattus norvegicus* to 3.5 Å resolution. The rat PepT2 protein shares 47% identity with human PepT1 and 83% identity with human PepT2 (fig. S1), making it an excellent model to understand mammalian proton-coupled peptide transport. An inhibitory nanobody was identified that stabilizes the ECD relative to the transport domain, establishing a method for structure determination of SLC transporters with dynamic accessory domains. In contrast to current structures, PepT2 adopts an outward open state, representing the transporter in the state primed for peptide and drug uptake from the renal filtrate. This previously unobserved conformation now enables a more complete model for alternating access transport to be proposed. In addition, the structure of PepT2, combined with molecular dynamics (MD) analysis

Copyright © 2021  
The Authors, some  
rights reserved;  
exclusive licensee  
American Association  
for the Advancement  
of Science. No claim to  
original U.S. Government  
Works. Distributed  
under a Creative  
Commons Attribution  
NonCommercial  
License 4.0 (CC BY-NC).

<sup>1</sup>Department of Biochemistry, University of Oxford, Oxford OX1 3QU, UK. <sup>2</sup>Dunn School of Pathology, University of Oxford, Oxford OX1 3RE, UK. <sup>3</sup>Central Oxford Structural Molecular Imaging Centre, University of Oxford, South Parks Road, Oxford OX1 3RE, UK. <sup>4</sup>Center for Structural Biology, Center for Cancer Research, National Cancer Institute, Frederick, MD 21702, USA. <sup>5</sup>Structural Biology, The Rosalind Franklin Institute, Harwell Science and Innovation Campus, Didcot, UK. <sup>6</sup>Division of Structural Biology, The Wellcome Centre for Human Genetics, University of Oxford, Oxford, UK. <sup>7</sup>Protein Production UK, The Research Complex at Harwell, Harwell Science and Innovation Campus, Didcot, UK. <sup>8</sup>The Kavli Institute for Nanoscience Discovery, University of Oxford, Oxford OX1 3QU, UK.

\*Corresponding author. Email: simon.newstead@bioch.ox.ac.uk (S.N.); joanne.parker@bioch.ox.ac.uk (J.L.P.); susan.lea@path.ox.ac.uk (S.M.L.); philip.biggin@bioch.ox.ac.uk (P.C.B.)

†These authors contributed equally to this work.

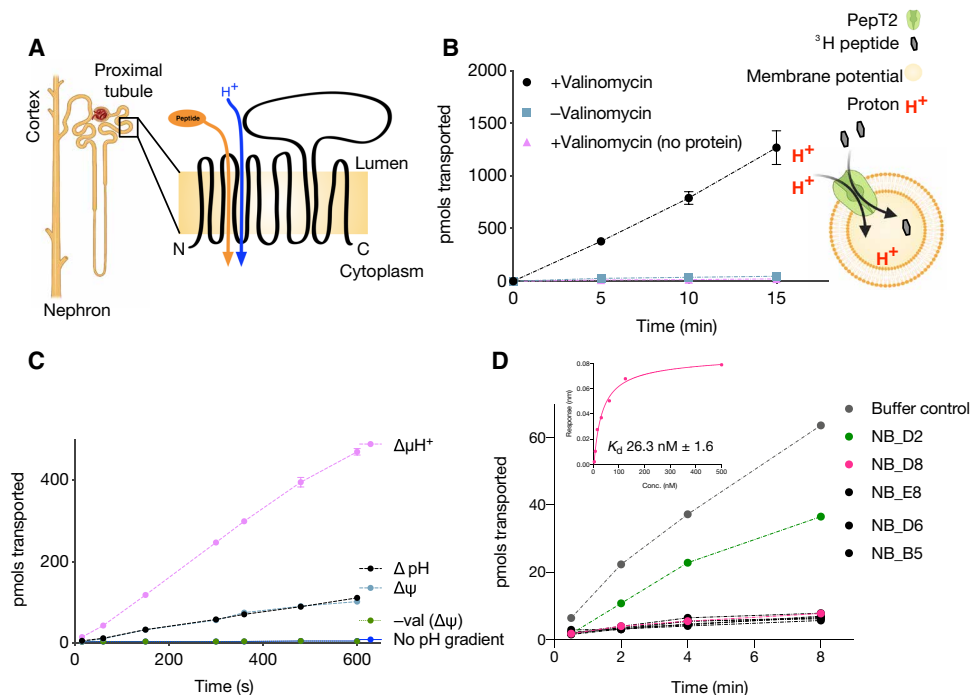


**Fig. 1. Functional characterization of PepT2 and the inhibitory nanobody D8.** (A) Location of PepT2 within the kidney (indicated by a box) and topology schematic of mammalian peptide transporters. (B) PepT2 reconstituted into liposomes can uptake peptide in the presence of a membrane potential generated through the presence of valinomycin. The schematic shows the experimental setup used. (C) PepT2 is a proton-driven peptide transporter being able to use a membrane potential ( $\Delta\psi$ , negative inside) or a pH gradient to drive peptide accumulation. The combination of both gradients ( $\Delta\mu\text{H}^+$ ) results in increased transport. (D) Most of nanobodies (NBs) raised against PepT2 lacking the extracellular domain (ECD) could inhibit peptide uptake. The NB referred to as D8 was the one used to solve the structure of PepT2. Inset: NB\_D8 has a dissociation constant ( $K_d$ ) of  $\sim 26$  nM for binding to full-length PepT2; a representative trace from the biolayer interferometry is shown with the calculated mean and SD ( $n = 3$ ).

of docked di- and tripeptide ligands, reveals the molecular basis for the extreme peptide promiscuity observed in the mammalian members of the SLC15 family. Thus, our results establish a model for understanding the role of mammalian SLC15 family transporters in peptide and prodrug transport across the plasma membrane.

## RESULTS AND DISCUSSION

### Identification of inhibitory nanobodies

To obtain the structure of a mammalian peptide transporter, we screened homologs from several different species to find a suitable target. The SLC15A2 homolog (PepT2) from the rat (*R. norvegicus*) was suitable for biophysical and biochemical characterization (fig. S2, A to D). Rat PepT2 showed robust proton-coupled transport in a reconstituted liposome system (Fig. 1B). We observed that either a pH gradient ( $\Delta\text{pH}$ ) or a membrane potential ( $\Delta\psi$ ) could drive transport and that the combination ( $\Delta\mu\text{H}^+$ ) is additive (Fig. 1C), consistent with electrogenic transport (14). Rat PepT2 transports a wide range of peptides and a diverse range of clinically relevant drugs and prodrugs (fig. S2, C and D). Attempts at either vapor diffusion or lipid cubic phase (LCP) crystallization did not yield crystals. However, single-particle cryo-electron microscopy (cryo-EM) provided promising 2D class averages yet failed to produce a high-resolution reconstruction despite the use of different sample preparation techniques, including different detergents, amphipols, and nanodiscs in the presence or absence of a substrate. We reasoned

that the failure to determine a high-resolution structure was due to the highly dynamic nature inherent to SLC transporters and the ECD specific to PepT2. To address this challenge, we sought to stabilize PepT2 through the addition of inhibitory nanobodies.

Initial attempts to obtain nanobodies were performed by immunizing against wild-type (WT) PepT2 reconstituted into liposomes. While this strategy was successful in generating specific nanobodies to the protein, all those tested were to the ECD of the transporter and none fully inhibited transport (fig. S2E). We therefore repeated immunization with reconstituted protein lacking the ECD ( $\Delta 410$ -603), which is still functional (fig. S2F). The engineered PepT2- $\Delta\text{ECD}$  generated several nanobodies that were capable of inhibiting transport, with the lowest dissociation constant ( $K_d$ ) of  $\sim 25$  nM obtained for nanobody D8 (Fig. 1D and fig. S2G). Through the formation of a stable complex of WT PepT2 with the inhibitory nanobody D8, we successfully obtained the structure of PepT2 through cryo-EM to 3.5 Å (Table 1).

### Cryo-EM structure of PepT2

PepT2 consists of two domains, a transmembrane (TM) domain that functions to couple peptide recognition to proton-driven transport and a large ECD inserted between TM9 and TM10 (Fig. 1A and fig. S1) (13). The cryo-EM maps were of sufficient quality to build the complete structure of PepT2 de novo (Fig. 2A and fig. S3). The TM domain adopts the canonical MFS fold, with helices TM1 to TM6 forming the N-terminal bundle and helices TM7 to TM12

**Table 1. Cryo-EM data collection, refinement, and validation statistics.**

| PepT2-NB (EMDB-12528) (PDB 7NQK)                    |           |           |
|---|-----------|-----------|
| <b>Data collection and processing</b>               |           |           |
| Magnification                                       | 105,000   | 105,000   |
| Voltage (kV)  | 300       | 300       |
| Electron exposure (e <sup>-</sup> /Å <sup>2</sup> ) | 59.1      | 56.9      |
| Defocus range (μm)                                  | 0.5–3.0   | 0.5–3.0   |
| Pixel size (Å)                                      | 0.832     | 0.832     |
| Symmetry imposed                                    | C1        | C1        |
| Initial particle images (no.)                       | 7,878,916 | 8,666,269 |
| Final particle images (no.)                         | 298,562   |           |
| Map resolution (Å)                                  | 3.5       |           |
| FSC threshold                                       | 0.143     |           |
| Map resolution range (Å)                            | 3.5–4.5   |           |
| <b>Refinement</b>                                   |           |           |
| Initial model used (PDB code)                       | None      |           |
| Model resolution (Å)                                | 3.5       |           |
| FSC threshold                                       | 0.143     |           |
| Model resolution range (Å)                          | 3.5–4.5   |           |
| Map sharpening B factor (Å <sup>2</sup> )           | –94.4     |           |
| <b>Model composition</b>                            |           |           |
| Nonhydrogen atoms                                   | 6139      |           |
| Protein residues                                    | 781       |           |
| Ligands   | 0         |           |
| <b>B factors (Å<sup>2</sup>)</b>                    |           |           |
| Protein   | 95.74     |           |
| Ligand  | N/A       |           |
| <b>Root mean square deviations</b>                  |           |           |
| Bond lengths (Å)                                    | 0.005     |           |
| Bond angles (°)                                     | 0.841     |           |
| <b>Validation</b>                                   |           |           |
| MolProbity score                                    | 2.22      |           |
| Clashscore  | 16.40     |           |
| Poor rotamers (%)                                   | 0.90      |           |
| <b>Ramachandran plot</b>                            |           |           |
| Favored (%)   | 91.38     |           |
| Allowed (%)   | 8.62      |           |
| Disallowed (%)                                      | 0.00      |           |

forming the C-terminal bundle. The ECD consists of two immunoglobulin G (IgG) domains that are linked in tandem and sits directly above the C-terminal bundle (Fig. 2B). The ECD makes only a single hydrogen bond to the transporter domain, through Arg<sup>553</sup> to the backbone carbonyl group of Asn<sup>328</sup> on TM7, which contains a large loop that extends out horizontally from the transporter before connecting to TM8. The inhibitory nanobody was clearly observed in the maps, with the CDR3 loop binding to side chains on TM1 and

TM2 from the N-terminal bundle and β strands 13 to 14 and the loop between β strands 10 and 11 on the second IgG-2 in the ECD (Fig. 2C and fig. S4B). This configuration explains why the nanobody was instrumental in determining the structure, as it functions to stabilize the TM helices and ECD, fixing them in a single state that could be used for high-resolution reconstruction.

Functionally, the ECD is thought to bind to extracellular trypsin, localizing the protease close to the TM domain to increase the efficiency of cationic peptide transport (13). An interesting question concerning the role of the ECD in mammalian peptide transport is whether this region is structurally rigid with respect to the transport domain or flexible, free to move around and capture nearby proteases. The structure reveals the latter model is more likely, as the ECD does not make any substantial contacts to the TM domain and is linked by flexible extensions from TM9 and TM10 (Fig. 2B). To test the degree of structural flexibility, we analyzed the movement of the ECD relative to the TM domain using MD (Fig. 3A). During MD simulations, we found that the ECD behaves as a rigid body with very little in the way of internal motions (fig. S5, A and B), consistent with previous studies on the isolated domain (13). Principal components analysis (PCA) on the trajectory demonstrates that most of the motion could be captured by the first four principal components (Fig. 3B), which can be assigned to translations in the *x*, *y*, and *z* axes and an additional rotation around the *z* axis (Fig. 3C). Our results show that the ECD does not occupy a fixed position with respect to the TM domain. Previously, we identified a potential binding site for trypsin (fig. S5C) (13), consisting of two conserved acidic side chains on the ECD (Asp<sup>576</sup> and Glu<sup>599</sup>). The MD analysis supports the accessibility of this site for trypsin binding and would position the protease above the transporter domain facilitating peptide transport.

On the cytoplasmic side of the transporter, inserted between the N- and C-terminal bundles, is an intracellular domain, consisting of 42 amino acids. This domain is predominantly α-helical and extends away from the transporter at an approximate 90° angle (Fig. 2B). At the distal end of a long lateral helix that constitutes the bulk of this domain are two arginine side chains, which our MD analysis shows to stabilize this domain on the intracellular side of the membrane (Fig. 3D and fig. S5D). A similar intracellular domain is observed in the distantly related plant nitrate transporter NRT1.1 (15, 16), where it functions as a binding platform for signaling proteins, including kinases and transcription factors (17). Although PepT2 is not known to function as a signaling system in mammalian cells, it is posttranslationally regulated through the binding of PDZK1 (Putative PDZ domain-containing protein kinase 1), a member of the Na<sup>+</sup>/H<sup>+</sup> exchanger regulator family of intracellular binding proteins (18). Binding of PDZK1 (NHERF3) to the C terminus of PepT2 results in a significant increase in the *V*<sub>max</sub> for peptide transport, which occurs under periods of high metabolic activity in the cell (19). The intracellular domain makes substantial interactions with TM7, a key gating helix in the MFS and sits close to the C terminus of TM12. Our structure thus suggests the kinetic effects observed following PDZK1 binding are likely to stem from modulation on the stability of TM7 and therefore affecting the gating dynamics of the transporter.

### Outward open conformation

Contrary to previous POT family transporter structures, which have all adopted an inward open or inward occluded state (12), PepT2 adopts an outward open conformation (Fig. 2A). A large polar cavity extends from the extracellular side of the membrane and

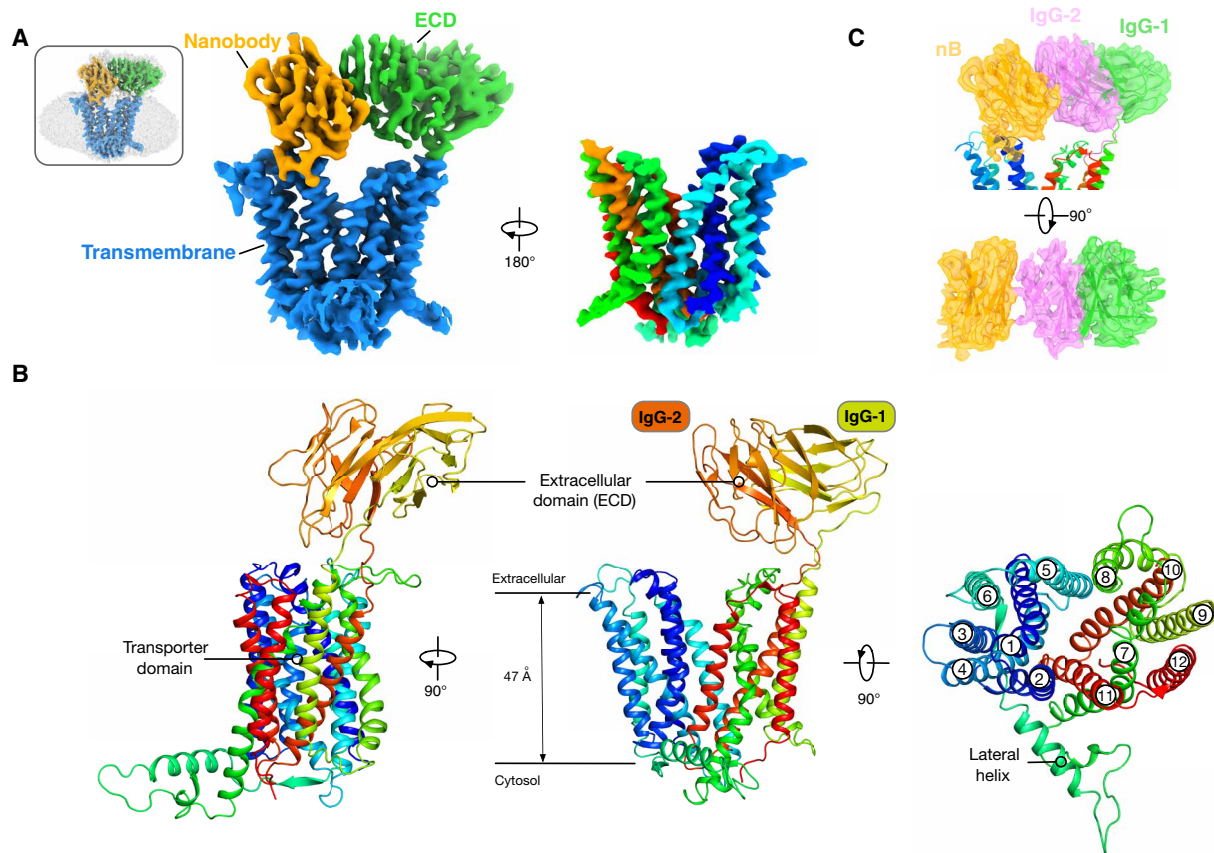


**Fig. 2. Cryo-EM structure of PepT2.** (A) Cryo-EM density of the PepT2 nanobody complex, contoured to a threshold level of 0.43. Left: The TM domain, ECD, and nanobody are represented in blue, green, and orange, respectively. Right: Rotated view of the TM domain, colored as rainbow. Inset: Superposition with lower contoured (threshold level of 0.13) volume to display the detergent micelle. (B) Cartoon representation of PepT2 highlighting the two domains, the membrane-embedded transport domain and the ECD composed of two IgG domains linked in tandem. (C) Cryo-EM density with overlaid model of ECD and nanobody. IgG-1 subdomain, IgG-2 subdomain, and nanobody are colored in green, violet, and orange, respectively. Map is contoured to a threshold level of 0.29.

reaches down  $\sim 37$  Å toward the intracellular gate, which is sealed to the inside of the cell (Fig. 4A). The intracellular gate is constructed by the close packing of the cytoplasmic ends of TM4 to TM5 with TM10 to TM11. The close packing of these four helices is stabilized through a salt bridge interaction between Asp<sup>170</sup> on TM4 and Lys<sup>642</sup> on TM11, both of which are strictly conserved within the mammalian and mammalian-like bacterial POT family members (Fig. 4B and fig. S1). In addition, several other side chains are conserved in this area of the protein and likely to facilitate the close packing of these helices. In particular, Pro<sup>162</sup> on TM4, which packs against Gln<sup>646</sup> on TM11, is located at the base of the binding pocket, acting as a pinch point in the transporter. A conserved feature of MFS transporters are pairs of salt bridge interactions that coordinate structural rearrangements during transport. In the extracellular gate, which is constructed from TM1 to TM2 and TM7 to TM8, a conserved histidine on TM1, His<sup>87</sup>, forms a salt bridge with Asp<sup>317</sup> on TM7, which drives closure of the extracellular gate following peptide and proton binding (Fig. 4C) (20). The identity of the intracellular gate salt bridge, however, has remained elusive, owing to a lack of structural information on an outward open state. Our structure now reveals that the intracellular gate salt bridge is located much further down the transporter, in a region that would be accessible to

the cytoplasm (Fig. 4C). This location is not the same as the previously suggested salt bridge interaction between a conserved lysine on TM4, Lys<sup>161</sup>, and glutamate on TM10, Glu<sup>622</sup> (12). To investigate the importance of the newly identified salt bridge between TM4 and TM11, we analyzed variants of these side chains using a cell-based transport assay (Fig. 4, D and E). An Asp<sup>170</sup>Ala variant resulted in loss-of-transport function, while still being expressed at the plasma membrane (fig. S6). Similarly, its interaction partner Lys<sup>642</sup> also displayed markedly reduced transport when mutated to alanine. These results confirm the importance of this salt bridge for coordinating structural rearrangements that result in opening the intracellular gate during transport. However, the location of the salt bridge on the cytoplasmic side of the transporter argues against a direct role in proton coupling or peptide binding. More likely, the role of this salt bridge is simply to stabilize the close packing of the intracellular gate helices in the outward open state. Last, a notable feature of the peptide binding site is a prominent dipole, which is located toward the bottom half of the cavity (Fig. 4B). The dipole is formed by Arg<sup>57</sup> on TM1 and Lys<sup>161</sup> on TM4, which sit opposite of Asp<sup>317</sup> on TM7 and Glu<sup>622</sup> on TM10. The dipole is a strictly conserved feature of the peptide binding site within the wider POT family and plays an important role in peptide recognition when the transporters

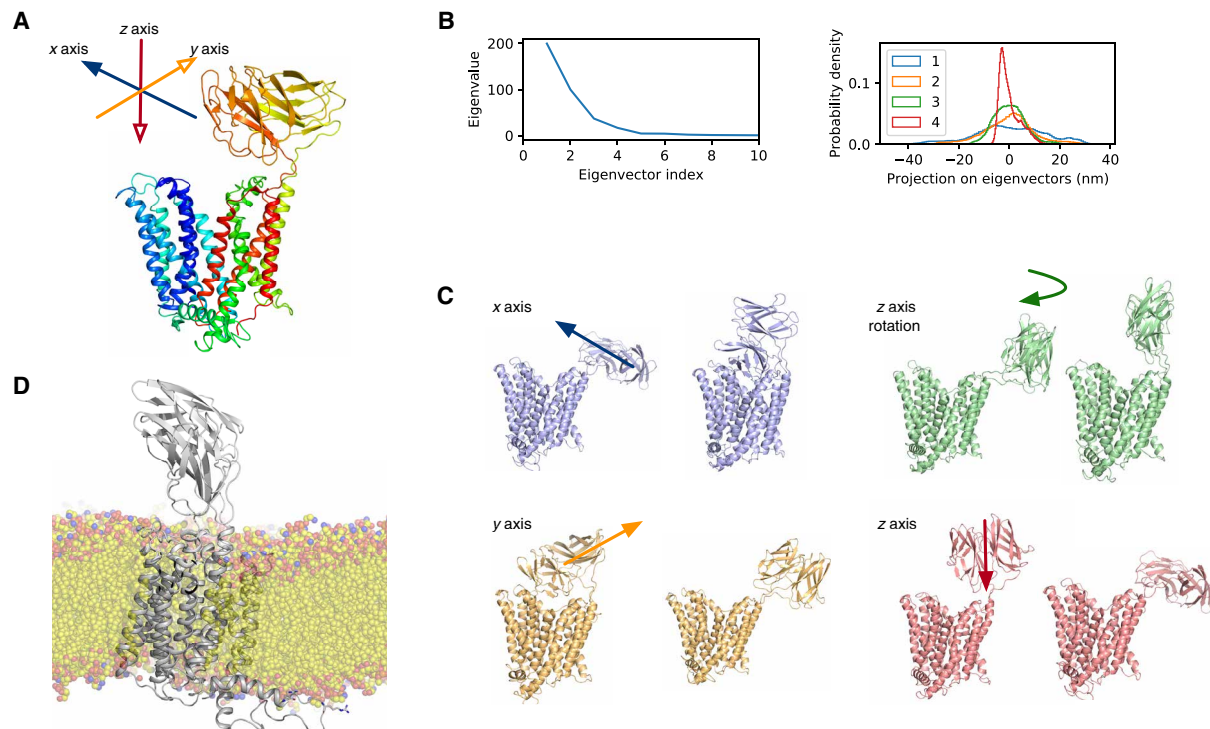


**Fig. 3. PCA of the dynamic movements of the ECD of PepT2.** (A) Decomposition of the ECD domain motion by PCA showing that most motion can be captured by the first four eigenvectors, shown in (B). Projections of the first four eigenvectors show that the motions are normally centered on the mean with no distinctive hotspots. (C) The first four motions can be classified as an *x*- or *y*-plane translation (purple and orange) and rotation along the *z* axis (green) and a *z*-axis translation (red), which can be summarized as translations in all three dimensions and a rotation of the IgG along the *z* axis with respect to the membrane. (D) Snapshot of the simulations showing PepT2 in a lipid bilayer and the role of the lateral helix in stabilizing the position of the transporter domain. The conserved arginine side chains on the lateral helix are shown (gray sticks).

adopt an inward-facing state (21, 22). As discussed below, these side chains also play essential roles in ligand recognition within the outward-facing state.

### Structural basis for ligand promiscuity

An important physiological function for intestinal peptide transporters is the bulk uptake and retention of dietary peptides (23). To achieve this function, both PepT1 and PepT2 have evolved to recognize a diverse library of di- and tripeptides, with upper estimates at >8000 different combinations being recognized (5). The availability of the outward open state of PepT2 now enables a detailed analysis of the peptide binding site at the start of the transport cycle. To understand how the binding site accommodates peptides of different length and size, we used MD to dock peptides into the binding site and supported these simulations with biochemical assays. We chose a small library of six peptides, where structural and biochemical information was already available from bacterial POT family homologs (21, 22, 24). Using a liposome-based assay, we calculated median inhibitory concentration ( $IC_{50}$ ) values for the six peptides (fig. S7D). The  $IC_{50}$  values were very similar, ranging from the tightest binding peptide L-Tyr-Tyr-Tyr (10  $\mu$ M) to the weakest binding peptide L-Phe-Ala (60  $\mu$ M). This result contrasts with peptide recognition in bacterial homologs, which show distinct preferences for smaller, hydrophobic dipeptides (24, 25) and suggests that PepT2, unlike its bacterial counterparts, does not discriminate based on peptide length.

To further understand peptide recognition, we used a strategy that combined docking with MD to predict the binding poses of dipeptides (L-Ala-Ala, L-Ala-Phe, and L-Phe-Ala) and tripeptides (L-Ala-Ala-Ala, L-Phe-Ala-Gln, and L-Tyr-Tyr-Tyr) (fig. S7A). AutoDock Vina (26) was used to generate initial docking poses for the peptides (fig. S7B), which were then relaxed through unbiased MD simulations. Representative binding poses were lastly obtained through clustering of four independent 100-ns-long trajectories for each peptide (fig. S7C). As a negative control, we used the amino acid L-alanine, which predictably failed to establish a stable binding position (fig. S8A), consistent with the inability of amino acids to inhibit transport (fig. S2C). In contrast, all di- and tripeptides established a stable binding pose after 100 ns (fig. S8, B to F). Next, we computed the absolute binding free energies (ABFE) based on these representative binding poses (fig. S7D). The calculated binding free energies correlated well with our previous  $IC_{50}$  values (Fig. 5A) {Spearman rank correlation:  $r_s = 0.9$ ,  $P = 0.04$ ; Pearson correlation coefficient [ABFE versus  $\log(IC_{50})$ ]:  $r = 0.83$ ,  $P = 0.08$ }, with the tightest binding peptide also being L-Tyr-Tyr-Tyr, with a calculated  $\Delta G$  at  $-26$  kcal mol $^{-1}$  compared to the worst binding peptide, Phe-Ala, at  $-7$  kcal mol $^{-1}$ .

All of the peptides adopted a similar position at the base of the binding site,  $\sim 31$  Å from the extracellular side of the membrane, with their N and C termini orientated with respect to the dipole within the cavity (Fig. 5B). A structural overlay of the peptides reveals a consistent pattern of interactions (Fig. 5C). Specifically, N termini

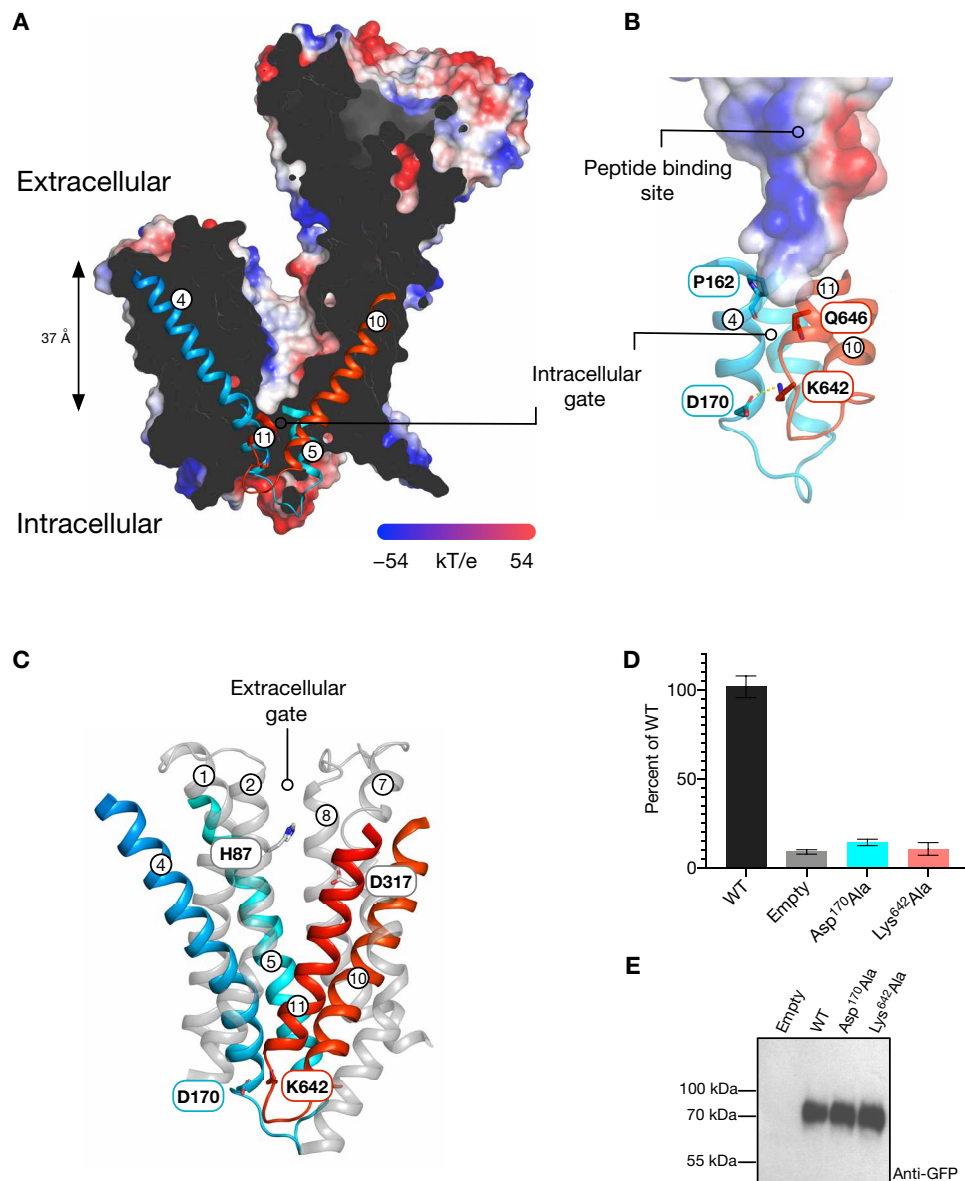


**Fig. 4. Outward open conformation of PepT2.** (A) Slice through the electrostatic surface representation of PepT2 as viewed in the plane of the membrane. The intracellular gating helices TM4 to TM5 and TM10 to TM11 are shown. (B) Zoomed-in view of the intracellular gate, with the key stabilizing interactions identified and labeled. (C) Cartoon representation showing the gating helices in PepT2. Key side chains involved in gate stabilization are shown. (D) Cell-based transport assays for PepT2 and variants of the intracellular gate-interacting side chains. (E) Western blot using an anti-green fluorescent protein (GFP) antibody to detect WT and variant forms of PepT2.

all interacted with the conserved glutamate on TM10 (Glu<sup>622</sup>) and through hydrogen bonds to two further strictly conserved asparagines on TM5 (Asn<sup>192</sup>) and TM8 (Asn<sup>348</sup>). At the opposite end of the peptides, we observed that all of the C termini interact with Arg<sup>57</sup>, which forms part of a conserved ExxER<sup>57</sup> motif on TM1 (24, 27). Both Arg<sup>57</sup> and Glu<sup>622</sup> are functionally critical side chains in the mechanism of proton-coupled peptide transport and variations of either abolish transport in both bacterial and mammalian members of the family (12). In addition to the conserved interaction at the N and C termini, all of the peptides project their N-terminal carbonyl groups toward Asn<sup>192</sup>. This enables the peptides to position the first side-chain group toward the binding site entrance, facilitating

optimal interactions between the N terminus, asparagines 192 and 348, and Glu<sup>622</sup> (Fig. 5D). The weakest binding peptide tested, L-Phe-Ala, is unable to adopt this pose. The position of the phenylalanine ring at the N terminus forces the peptide bond to rotate almost 180° relative to the other peptides, forcing the carbonyl group to extend toward the opening of the binding site. In this position, the carbonyl group is unable to interact with Asn<sup>192</sup>, and, subsequently, the tight interaction network is lost. The reduced interactions observed in the simulations explain why the presence of a carbonyl group close to the N terminus is a key determinant of high affinity binding to the mammalian transporters, as the carbonyl group acts to stabilize the interactions around the N terminus of the peptide ligands.

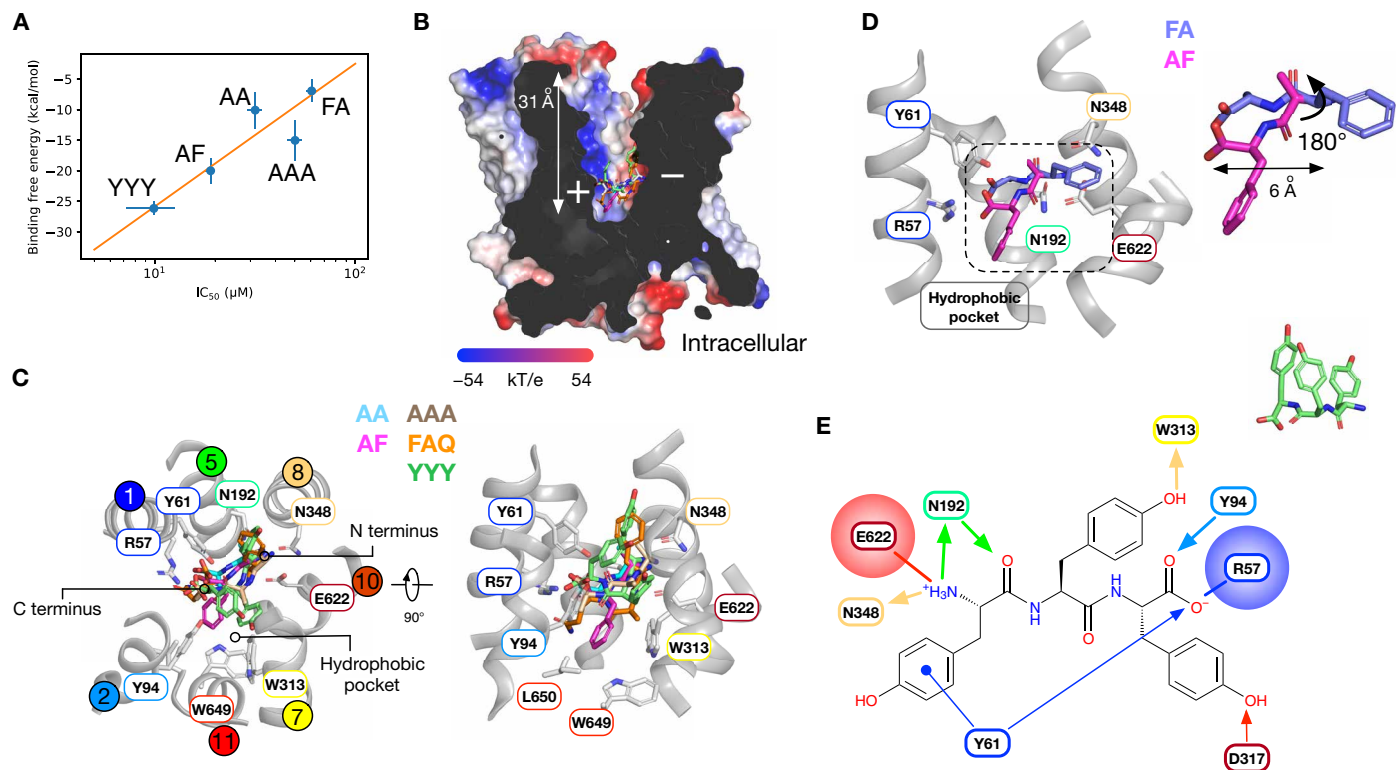


**Fig. 5. Peptide binding to PepT2.** (A) Correlation between  $IC_{50}$  values and ABFE [Spearman rank correlation:  $r_s = -0.9$ ,  $P = 0.04$ ; Pearson correlation coefficient, ABFE versus  $\log(IC_{50})$ :  $r = -0.83$ ,  $P = 0.08$ ]. (B) Slice through the electrostatic surface representation of PepT2, with the peptides shown overlaid in the binding site. (C) Close-up view of the binding site shown in (B). The five peptides are shown as different colored sticks, with key side chains shown in sticks and labeled. Side-chain positions are taken from the cryo-EM structure. (D) Zoomed-in view of the binding site showing the different binding poses for L-Ala-Phe (magenta) and L-Phe-Ala (purple). (E) Schematic of the peptide binding site, highlighting the key structural features (see text) for Tyr-Tyr-Tyr recognition. The final binding pose for Tyr-Tyr-Tyr is shown at the inset, top right. Arrows indicate direction of hydrogen bonds, with ionic interactions depicted as straight lines.

Previous studies on the bacterial homologs had identified several specificity pockets that accommodate different side-chain groups (21, 22) and highlighted the role of conserved tyrosine side chains in creating a promiscuous binding site (28). In particular, a conserved hydrophobic pocket was observed to form around the phenylalanine in the L-Ala-Phe complex with PepT<sub>St</sub> (21). We observe similar pockets in the outward-facing state PepT2 (Fig. 5C), and our MD docking predicts an almost identical binding pose for the Ala-Phe peptide, with the phenylalanine side chain pointing toward the same hydrophobic pocket (Fig. 5D). This result suggests that the peptide is likely to remain stable during transport, with the transporter moving around the peptide.

Peptides interact with proteins in a wide variety of ways but are frequently held in an extended conformation, as observed previously in OppA, calmodulin, and major histocompatibility complex class I and class II molecules (29). A key question we wanted to address was how larger peptides, such as L-Tyr-Tyr-Tyr, are accommodated in PepT2, as these are similar in size to drug and prodrug ligands, such as cefadroxil and valacyclovir (30). Unlike the Phe-Ala peptide, where we observe the phenylalanine side chain binding into the hydrophobic pocket, the tyrosine side chains adopt a vertical orientation, in a crown-like arrangement (Fig. 5E). Specific interactions are made to conserved side chains—Tyr<sup>61</sup>, Tyr<sup>94</sup>, and Trp<sup>313</sup>—via hydrogen bonds. Unlike the Phe-Ala peptide, however, the first side chain does not orientate toward Glu<sup>622</sup>. Instead, the first tyrosine

side chain interacts with Tyr<sup>61</sup> through both a hydrogen bond and a  $\pi$ - $\pi$  stacking interaction. Tyrosine-61 also coordinates the C terminus, helping to clamp the large peptide in place. Together, a substrate binding model for the outward open state of the mammalian SLC15 family can be summarized (Fig. 5E). The key features of this model build on earlier work (21, 22, 31–33) and confirm the critical importance of conserved acidic (Glu<sup>622</sup>) and basic (Arg<sup>57</sup>) side chains that clamp the N and C termini in place, respectively, with an ideal distance between these two interaction sites being 6 Å. The first carbonyl group is important for discriminating between high- and low-affinity ligands through the interaction with a conserved hydrogen bond donor (Asn<sup>192</sup>), which also coordinates the N terminus by acting as a hydrogen bond acceptor. In addition, the peptide binding poses explain how diverse side chains are accommodated through the presence of conserved aromatic residues (Tyr<sup>61</sup>, Tyr<sup>94</sup>, and Trp<sup>313</sup>), which can also contribute to hydrophobic and polar pockets where needed. Similar mechanisms of recognition have been observed in OppA, the periplasmic binding protein from the oligopeptide adenosine triphosphate-binding cassette transporter Opp, and the transporter associated with antigen processing (TAP). In these systems, which exhibit similar extreme promiscuity, peptide side chains are accommodated in cavities that are not sequence specific (34), whereas peptide length is also constrained through salt bridges to the N and C termini (35, 36). Last, the comparison between the outward open state of PepT2 and the inward open bacterial

structures suggests that peptides are held rigidly, acting as a fulcrum around which the gating helices move during transport.

### Initial engagement of peptides with the binding pocket is via N-terminal interactions

Given that all of the di- and tripeptides interacted with PepT2 via both their N and C termini, we sought to understand to what extent each terminus contributes to the binding mode and understand the likely sequence of peptide engagement. L-Ala-Ala-Ala was chosen as our model ligand because of its medium size and inert side chains. Potential of mean force (PMF) calculations show that engagement via the N terminus first yields a favorable free energy landscape, compared to an initial engagement via the C terminus (Fig. 6A). To gain a better understanding of the preference for the initial N-terminal engagement, we examined the interactions the peptide made with the binding site using MD. Binding proceeds via a hopping mechanism with the N terminus initially forming a salt bridge with Asp<sup>317</sup> before transferring to Glu<sup>622</sup> (Fig. 6B). In this position, the N terminus makes further interactions with Asn<sup>192</sup> and Asn<sup>348</sup>, creating a stable binding pose ( $\sim -5$  kcal/mol) that firmly locks the N terminus in place (Fig. 6C), confirming our previous docking results. Following N terminus binding, the C terminus interacts initially with Lys<sup>64</sup> on TM1 before adopting its final position close to Arg<sup>57</sup>. The final stable binding pose is facilitated through interactions with the conserved tyrosine side chains within the binding site (Fig. 6D and movie S1) as described in our binding model.

### Structural analysis of inward and outward open states

MFS transporters contain a canonical 12 TM fold, which can be split into two six-helix bundles (Fig. 7A). Alternating access transport is thought to occur following the movement of these two bundles around a central binding site, although mechanistic differences are common between subfamilies of MFS transporters (37, 38). Although

the POT family has been extensively studied, all current structures of bacterial members were captured in the inward open state, hampering efforts to understand the mechanism of alternating access transport within this family. The structure of PepT2 reported here now enables a detailed analysis of the key structural changes that occur during proton-coupled peptide transport. Previously, we identified a closely related mammalian-like bacterial homolog of the mammalian peptide transporters, PepT<sub>So</sub> (28), and determined its structure to high resolution using LCP crystallization [Protein Data Bank (PDB): 4UVM] (39). Using the inward open structure of PepT<sub>So</sub>, we analyzed the major conformational differences between the two structures to gain insight into the structural changes that occur during alternating access transport in the POT family. The superimposition reveals that the main structural changes between the outward- and inward-facing states of the two transporters reside in the N-terminal six-helix bundle, with very little structural change observed in the C-terminal bundle helices (Fig. 7B). The structural overlay reveals that TM1 and TM2 move toward TM7 and TM8, consistent with previous models for closure of the extracellular gate (39). TM1 and TM2 pivot forward  $\sim 35^\circ$  in the inward open state relative to the outward open state, with the hinge point sitting close to Tyr<sup>94</sup> on TM2 and Arg<sup>57</sup> and Tyr<sup>61</sup> on TM1. Similarly, TM4 and TM5 swing away in the opposite direction at  $\sim 42^\circ$ , with the hinge point at Lys<sup>161</sup>, a conserved site of proton binding in the N-terminal bundle (24, 27). In the C-terminal bundle, we observe that TM11 rotates  $\sim 24^\circ$  between the inward- and outward-facing states, and TM7 bulges near to Asp<sup>317</sup>. Unexpectedly, the small movements in the C-terminal bundle are inconsistent with previous transport models based on ligand-bound structures of PepT<sub>St</sub>, another bacterial homolog (21, 24). However, we have previously shown that PepT<sub>So</sub> and PepT<sub>St</sub> operate via different mechanisms, with PepT<sub>St</sub> able to couple transport di- and tripeptides to different numbers of protons, whereas PepT<sub>So</sub> operates using a single mechanism (20, 40). A

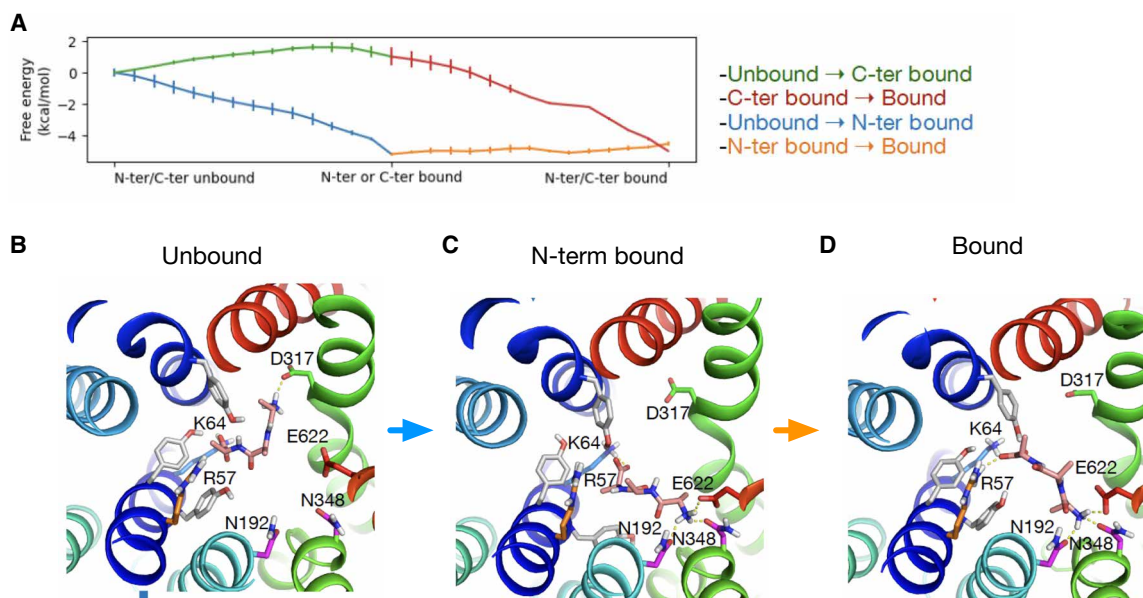


**Fig. 6. Binding of Ala-Ala-Ala proceeds via N-terminal engagement followed by C-terminal engagement.** (A) Free energy calculations show that N-terminal engagement followed by C-terminal engagement is more energetically favorable. (B) The N terminus of Ala-Ala-Ala initially interacts with Asp<sup>317</sup> before transferring to Glu<sup>622</sup> and is further coordinated by Asn<sup>192</sup> and Asn<sup>348</sup>. (C) Once the N terminus has formed a stable interaction, the C terminus engages with Arg<sup>57</sup> from Lys<sup>64</sup> and the movement is smoothed by Tyr<sup>60</sup>, Tyr<sup>61</sup>, and Tyr<sup>64</sup>. (D)



similar structural analysis comparing PepT2 to PepT<sub>St</sub> reveals a different result to one obtained with PepT<sub>So</sub> (fig. S9). When using PepT<sub>St</sub> as the comparator, the main structural movements occur in the C-terminal bundle. We conclude from this analysis that, in keeping with two thermodynamic mechanisms of proton-coupled peptide transport, there likely exist at least two different mechanisms for structural changes within the POT family. These are the non-mammalian-like POT members, which are characterized by structural movements in the C-terminal domain, and the mammalian or mammalian-like bacterial homologs, which operate using a different mechanism where structural changes occur mostly in the N-terminal domain.

### A model for proton-coupled transport by PepT2

The outward open structure of PepT2 reveals an important missing link in our understanding of alternating access within the POT family. Together with previous biochemical and structural studies on POT family peptide transporters, our current work enables a clearer understanding for a transport mechanism within the mammalian SLC15 family, which we have summarized in Fig. 8. In the outward-facing state, the transporter exposes a large polar cavity to the extracellular side of the membrane, which displays a strong dipole between the N- and C-terminal bundles. A conserved histidine on TM2, His<sup>87</sup>, is solvent accessible and protonated (i). A peptide enters the transporter via its N terminus, which is attracted to the

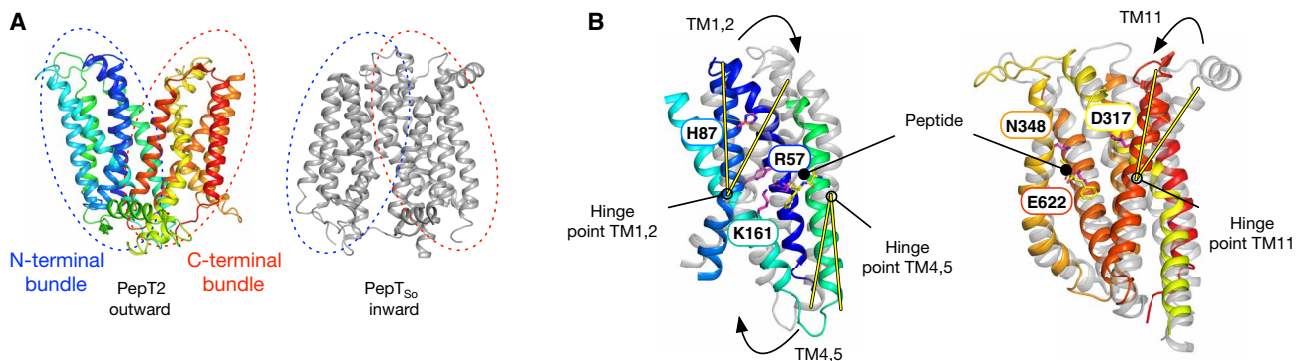


**Fig. 7. Transport mechanism of PepT2.** (A) Cartoon representation of PepT2 in the outward open state compared to PepT<sub>So</sub> (PDB: 2XUT) in the inward open state. The N- and C-terminal six-helix bundles are marked with blue and red dotted lines, respectively. (B) Structural overlay of the N-terminal bundle (left) and C-terminal bundle (right) colored as in (A). The key structural changes in the N-terminal bundles are highlighted by yellow lines, showing the angles of movement in TM2, TM4, and TM11. Key side chains involved in peptide and proton binding are indicated (purple sticks) and labeled. The docked L-Ala-Phe peptide is shown for reference.

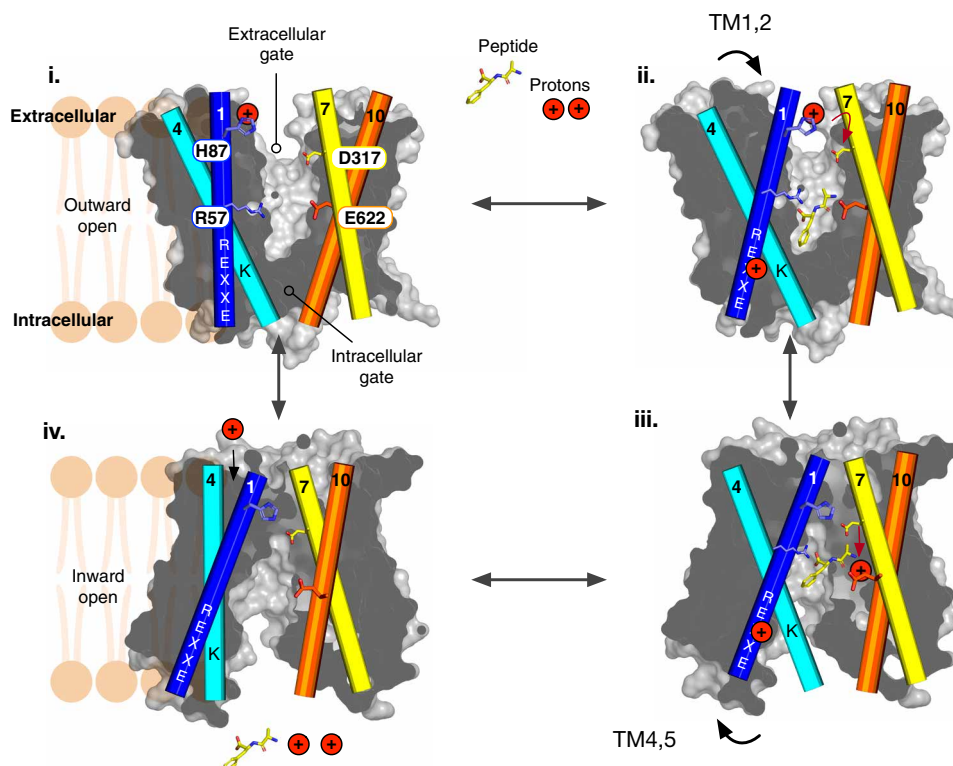


**Fig. 8. Alternating access transport mechanism within the SLC15 family.** Schematic representation of the transport cycle for PepT2, detailed in the main text.

solvent-exposed aspartic acid on TM7, Asp<sup>317</sup>. The peptide then moves down into the transporter, hopping from Asp<sup>317</sup> to Glu<sup>622</sup>, a strictly conserved side chain on TM10 (movie S1). In this position, the peptide orientates within the binding site under the influence of the dipole, with the C terminus interacting with Arg<sup>57</sup>, part of the conserved ExxER<sup>57</sup> motif on TM1 (ii) (Fig. 5). Side chains are accommodated within the various polar pockets, and conserved tyrosine side chains spread around the binding site. Once locked in place, TM1 to TM2 will move toward TM7 to TM8, closing the extracellular gate and stabilized by the interaction between His<sup>87</sup> and Asp<sup>317</sup>. In this occluded state, the proton on His<sup>87</sup> will transfer down, through Asp<sup>317</sup> to Glu<sup>622</sup> (iii). Proton binding to Glu<sup>622</sup> will disrupt the interaction with the N terminus of the peptide. At the opposite end of the binding site, protonation of the conserved ExxER<sup>57</sup> motif will lead to disruption of the interactions with Lys<sup>127</sup> that hold TM4 to TM5 in place, enabling these helices to swing away and release both peptide and protons into the cytoplasm (iv). In the inward open state, a water-filled channel that forms from the extracellular side of the transporter down toward His<sup>87</sup> enables the reprotonation of this side chain, weakening the interaction with TM7, and initiating the reorientation of the transporter to the outward-facing state, completing the cycle (i). This model assumes that neutral peptides are transported with two protons in the mammalian proteins, which we also propose is the minimal number for cotransport and consistent with previous electrophysiological studies (14, 41).

### Prodrug recognition

Last, we wanted to explore how PepT2 would interact with prodrug molecules. To date, crystal structures of bacterial POT transporters PepT<sub>Sh</sub>, from *Staphylococcus hominis* (PDB: 6GZ9), and DtpA, from *Escherichia coli* (PDB: 6GS4), have been reported in the inward open state and in complex with valacyclovir and valganciclovir, respectively (42, 43). Valacyclovir is a prodrug derivative of the antiviral agent acyclovir, which is used in the treatment of herpes virus and in the suppression of latent disease (44). Valacyclovir consists of an L-valine amino acid attached to the active acyclovir drug through an ester linkage, which creates a molecule that is recognized and transported by both PepT1 and PepT2 (7, 45). Valganciclovir was developed later to treat cytomegalovirus infections in patients with HIV/AIDS or following organ transplant (46) and differs in the presence of a methoxy group attached to the ester linkage. However, in the structure of DtpA, valganciclovir adopts a notably different pose to that of valacyclovir in PepT<sub>Sh</sub>, flipped ~180° (47). Therefore, to probe the binding pose of valacyclovir in PepT2, we docked the prodrug using the binding poses from both PepT<sub>Sh</sub> and DtpA. However, valacyclovir only yielded a stable binding pose in a position similar to that observed in PepT<sub>Sh</sub>. We were unable to identify a binding pose similar to that observed in DtpA for valganciclovir. However, we previously postulated that DtpA might recognize prodrugs differently to the mammalian peptide transporters due to the presence of a pronounced discontinuity in TM10, which changes the size and

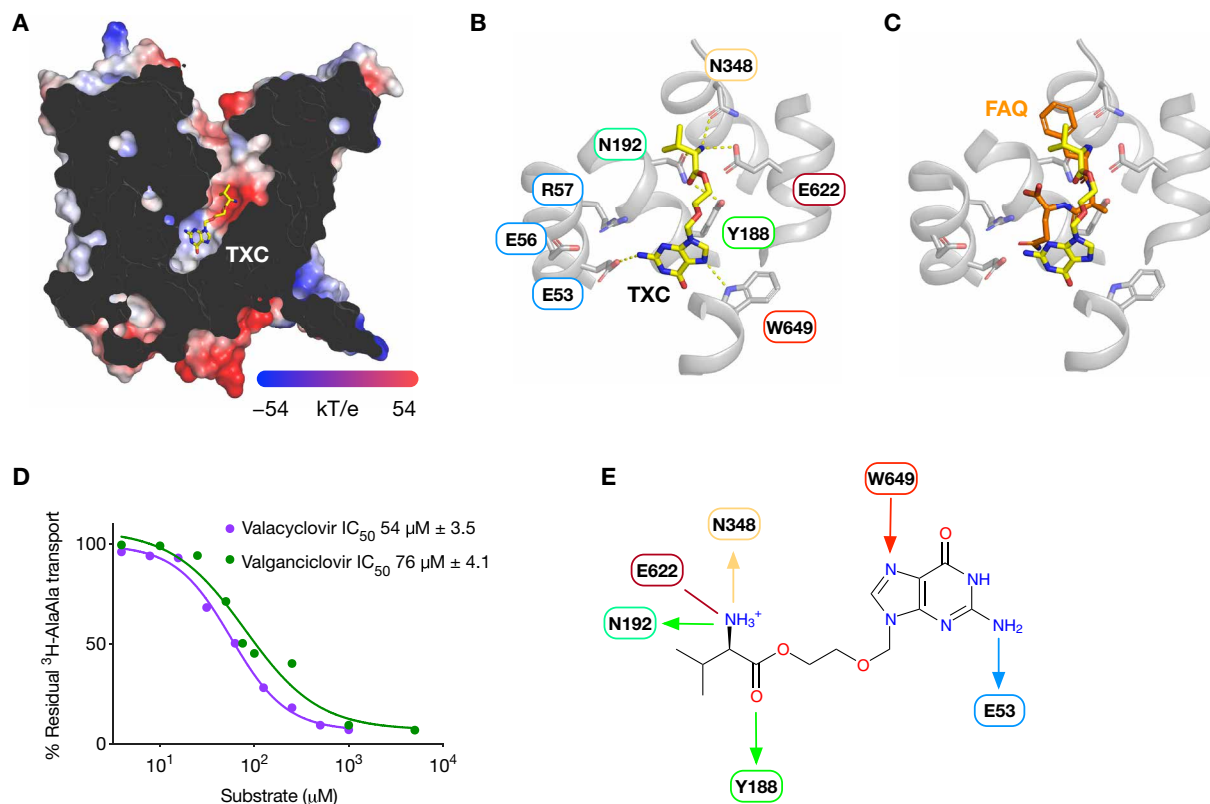


**Fig. 9. Model for prodrug recognition by PepT2.** (A) Slice through the electrostatic surface representation of PepT2, showing the location of valacyclovir (PDB: TXC) docked into the peptide binding site. (B) Close-up view of the binding site shown in (A). (C) Structural overlay of the L-Phe-L-Ala-L-Gln peptide on the valacyclovir binding pose. (D) Representative IC<sub>50</sub> curves for valacyclovir and valganciclovir reporting calculated means and SD ( $n = 3$ ). (E) Schematic of valacyclovir binding site, highlighting the key structural features in prodrug recognition. Arrows indicate direction of hydrogen bonds, with ionic interactions depicted as straight lines.

shape of the binding site (47). In PepT2, TM10 adopts a standard helical configuration (Fig. 2), which likely explains the difference in binding positions between these two proteins.

Valacyclovir (PDB: TXC) sits in an elongated state in the binding pocket (Fig. 9A), with the positively charged amino group of the L-valine moiety making hydrogen bond interactions with Glu<sup>622</sup>, Asn<sup>192</sup>, and Asn<sup>348</sup> (Fig. 9B), similar to the peptide ligands discussed above (Fig. 5C). The carbonyl group interacts with Tyr<sup>188</sup> on TM5, which forms part of the highly conserved POT family PTR2\_2 motif (FYxxINxG<sup>194</sup>), which plays an important role in peptide transport (48). Unlike the complex with PepT<sub>Sh</sub>, we did not observe any interactions to either the ester or ether groups in the drug. However, the primary amine of the purine ring forms a stable hydrogen bond with Glu<sup>53</sup>, while the imidazole interacts with the Trp<sup>649</sup>. Glu<sup>53</sup> forms part of the conserved ExxER<sup>57</sup> motif on TM1 and plays a central role in proton coupling, while Trp<sup>649</sup> on TM10 is part of the intracellular gate in the POT family (24). Superimposing the drug-bound structure reveals a notable similarity to the position of the tripeptide L-Phe-L-Ala-L-Gln [root mean square fluctuation (RMSF) of 0.8 Å], particularly with respect to the free N terminus of the amino acid (Fig. 9C). At the other end of the drug molecule, the amine group of acyclovir sits close to the side-chain carbonyl of L-Gln in the tripeptide, suggesting that the interaction with the ExxER<sup>57</sup> motif is a conserved and necessary feature of ligand recognition. This binding pose would also accommodate valganciclovir, with the methoxy group extending out toward Tyr<sup>61</sup>, which, as discussed above, also plays a role in peptide binding. IC<sub>50</sub> values for both prodrugs are similar (Fig. 9D), suggesting that the drugs interact with PepT2 in an analogous manner.

Together, the interactions identified as playing important roles in valacyclovir binding are consistent with those identified for the physiological peptide ligands (Fig. 9E) (4, 31). In particular, the prodrug binding model identifies the importance of the free N-terminal  $\alpha$ -amino group of the L-valine conjugate in recognition and transport. This requirement appears to extend to  $\beta$ -lactam antibiotics, as those without a free amino group show substantially reduced or, in many cases, no transport by PepT1 or PepT2 (4). In conclusion, the structure of the outward open state of PepT2, coupled with the insights into peptide and prodrug recognition, now enable a more rationalized approach to drug and prodrug design, targeting the intestinal and renal peptide transporters.

## MATERIALS AND METHODS

### Expression and purification

PepT2 (SLC15A2) from *R. norvegicus* (I.M.A.G.E. clone p970C0364D) was cloned into a modified pLexM vector (49) that contained a C-terminal His-tagged green fluorescent protein (GFP) with a TEV cleavage site between PepT2 and the GFP. The ECD was removed through overlap polymerase chain reaction (PCR), which removed amino acids 410 to 603, and cloned into plexm-tev-GFPHis. The plasmid is available through Addgene (167988).

The plasmids containing PepT2 were transiently transfected into human embryonic kidney-293F cells in the FreeStyle 293 Expression Medium (Thermo Fisher Scientific, UK). The cells were cultured in suspension phase at 37°C and 8% CO<sub>2</sub>. Eighteen to 24 hours before transfection, cells were passed at a density of  $7 \times 10^5$  cells/ml to give a density of  $1.3 \times 10^6$  to  $1.4 \times 10^6$  cells/ml at transfection. For the 2-liter culture, 2 mg of plasmid DNA was diluted in Dulbecco's

modified Eagle's medium (Thermo Fisher Scientific, UK) to a total volume of 30 ml, it was mixed gently and left to stand for 5 min. In that time, 4 ml (from 1 mg/ml of stock) of linear polyethyleneimine (PEI) MAX (MW 40,000; Polysciences Inc., USA) was diluted in the same medium to a volume of 30 ml in a separate tube and mixed. The diluted PEI MAX was added to the diluted DNA and mixed gently. The mixture was incubated for 10 to 15 min at room temperature and was added dropwise to the cells with gentle swirling. Sodium butyrate was then added at 8 mM final concentration. Cells were returned to the incubator and harvested 36 hours after transfection and frozen until required.

The cell pellet was thawed and resuspended in ice-cold phosphate-buffered saline (PBS) containing deoxyribonuclease, and cells were subsequently lysed using a sonicator (Qsonica, USA), 8 cycles of 30-s on followed by 60-s off on ice. Unbroken cells and cell debris were pelleted at 10,000g for 10 min at 4°C, and membranes were harvested through centrifugation at 200,000g for 1 hour and washed once with 20 mM Hepes (pH 7.5) and 20 mM KCl. After washing, the membranes were resuspended in PBS and snap-frozen for storage at -80 until required.

Membranes were thawed and solubilized in 1× PBS, 150 mM NaCl, and 10% glycerol containing 1% *n*-dodecyl- $\beta$ -D-maltopyranoside (DDM):cholesterol hemisuccinate (CHS) (5:1 ratio) for 90 min at 4°C. Insoluble material was removed through centrifugation for 1 hour at 200,000g. PepT2 was purified to homogeneity using standard immobilized metal affinity chromatography protocols in DDM detergent (Glycon, DE) with CHS (5:1 ratio DDM:CHS). Following TEV cleavage, the protease and cleaved His-tagged GFP were removed through nickel affinity chromatography, and the protein was subjected to size exclusion chromatography (Superdex 200) in a buffer consisting of 20 mM Tris (pH 7.5) and 150 mM NaCl with 0.03% DDM and 0.006% CHS. Biotinylated PepT2 was produced by adding a C-terminal Avi tag before the TEV cleavage site within the vector. The protein was purified as for WT, following biotinylation by BirA overnight, the protein was subjected to a further size exclusion run.

### Reconstitution into liposomes

PepT2 was reconstituted into liposomes consisting of a 3:1 palmitoyloleoylphosphatidylethanolamine:1-palmitoyl-2-oleoyl-*sn*-glycerol-3-phospho-(1'-rac-glycerol) (POPE:POPG) using biobeads following procedures previously described (50). Chloroform was removed from the lipids (Avanti Polar Lipids, USA) through the use of a rotary evaporator to obtain a thin film. The lipids were washed twice in pentane and then resuspended at 12 mg ml<sup>-1</sup> in lipid buffer [50 mM potassium phosphate (pH 7.5)]. These lipid vesicles were frozen and thawed twice in liquid nitrogen and stored at -80°C until required. For reconstitution, the lipids were thawed and then extruded first through a 0.8- $\mu$ m filter and then through a 0.4- $\mu$ m filter. Purified PepT2 in DDM:CHS (at 0.3  $\mu$ g  $\mu$ l<sup>-1</sup>) was added to the lipids at a final lipid:protein ratio of 100:1 and incubated for 1 hour at room temperature and then for a further 1 hour on ice; for the no-protein liposome control, the same volume of gel filtration buffer containing 0.03% DDM and 0.006% CHS was added. After this time, biobeads were added in batches over 24 hours. Biobeads were removed, and the proteoliposomes were harvested by centrifugation at 120,000g for 40 min before resuspension in lipid buffer at a final protein concentration of 0.25  $\mu$ g  $\mu$ l<sup>-1</sup>. They were subjected to three rounds of freeze-thawing in liquid nitrogen before storage at -80°C. The

amount of protein (both WT and mutant variants) reconstituted into the lipids was quantified by SDS–polyacrylamide gel electrophoresis (PAGE) and densitometry. For immunization into llamas to raise nanobodies, either 0.6 mg of full-length ECDA or 0.6 mg of PepT2\_ECDA was reconstituted into POPE:POPG (3:1) ratio at a lipid:protein ratio of 50:1 and resuspended at a final protein concentration of 0.8 mg/ml using the same method outlined above.

### Transport assays

Transport assays were performed following procedures previously described in (50). Proteoliposomes were thawed, and the required amount of proteoliposomes was harvested through centrifugation before resuspending in inside buffer [typically 120 mM potassium acetate, 2 mM MgSO<sub>4</sub>, and 20 mM Hepes (pH 7.5)]. The liposomes were subjected to four rounds of freeze-thawing in liquid nitrogen to fully distribute the buffer and then extruded through a 0.2- $\mu$ m filter. The proteoliposomes were diluted into the desired external buffer [typically 120 mM NaCl, 2 mM MgSO<sub>4</sub>, and 20 mM Hepes (pH 7.5)] containing peptide and trace amounts of <sup>3</sup>H di-alanine or in the presence or absence of 1  $\mu$ M valinomycin. The reaction was incubated at 30°C and stopped by rapidly filtering onto 0.22- $\mu$ m filters, which were then washed with 2  $\times$  2 ml of cold water. The amount of peptide transported inside the liposomes was calculated by scintillation counting in Ultima Gold (PerkinElmer) with comparison to a standard curve for the substrate. Experiments were performed a minimal of three times to generate an overall mean and SD.

### Details of specific experiments

Experiments to show proton-coupled uptake (Fig. 1B) used 1  $\mu$ g of protein per time point, and the inside buffer was 120 mM potassium chloride, 2 mM MgSO<sub>4</sub>, and 20 mM Hepes (pH 7.5). The outside buffer consisted of 120 mM NaCl, 2 mM MgSO<sub>4</sub>, and 20 mM Hepes (pH 7.5 or 6.8), with 1  $\mu$ M valinomycin where required. Experiments in Fig. 1C used 0.4  $\mu$ g of protein per time point. The buffers for  $\Delta\mu\text{H}^+$  consisted of 120 mM potassium acetate, 2 mM MgSO<sub>4</sub>, and 20 mM Hepes (pH 7.5) for the inside buffer and 120 mM sodium chloride, 2 mM MgSO<sub>4</sub>, and 20 mM Hepes (pH 7.5) for the outside buffer in the presence of valinomycin. For  $\Delta\text{pH}$ , acetate-induced pH gradients were used, and the outside buffer was 120 mM potassium chloride, 2 mM MgSO<sub>4</sub>, and 20 mM Hepes (pH 7.5) or 120 mM potassium acetate as the no pH control. For  $\Delta\psi$ , the inside buffer was 120 mM potassium chloride, 2 mM MgSO<sub>4</sub>, and 20 mM Hepes (pH 7.5), and the outside buffer was 120 mM sodium chloride, 2 mM MgSO<sub>4</sub>, and 20 mM Hepes (pH 7.5), with valinomycin to generate the membrane potential or no valinomycin as the control.

To test inhibition of transport by nanobodies, the nanobodies were included at 500  $\mu$ M in the inside and outside buffers with 0.5  $\mu$ g of PepT2 used per time point. Transport was driven only using a membrane potential generated through valinomycin. For the pH optimum experiments, 0.5  $\mu$ g of protein was used per time points and a final concentration of 50  $\mu$ M di-alanine with trace amounts of <sup>3</sup>H di-alanine. The internal buffer was 120 mM potassium chloride, 2 mM MgSO<sub>4</sub>, and 20 mM of the desired buffer, and external buffers used consisted of 120 mM NaCl, 2 mM MgSO<sub>4</sub>, and 20 mM buffer. The buffers used were MES (pH 6.0 to 6.5) or Hepes (pH 7.0 to 8.0) and tris for pH 8.5. Competition assays used  $\Delta\mu\text{H}^+$  to drive transport for 4 min, with the competing substrate present at 100  $\mu$ M or at varying concentrations to calculate the IC<sub>50</sub>. Counterflow experiments were performed using a buffer consisting of 50 mM sodium chloride, 2 mM MgSO<sub>4</sub>, and 20 mM Hepes (pH 7.5) on both the

inside and outside. The inside contained 1 mM of the potential substrate of interest and the outside contained 25  $\mu$ M di-alanine with trace amounts of <sup>3</sup>H di-alanine. One microgram of protein was used per experiment, and the reaction was stopped after 4 min.

### Cell-based peptide uptake assays

Transport assays were carried out with transiently transfected HeLa cells, which were cultured in RPMI 1640 medium (supplemented with 10% fetal bovine serum, 2 mM L-glutamine, and the Gibco MEM Non-Essential Amino Acids) under 5% CO<sub>2</sub> at 37°C. To transfect a 12-well plate, 2  $\times$  10<sup>5</sup> cells were seeded per well and, 24 hours later, transfected using Lipofectamine 2000 with PepT2 constructs in the vector plexm-tev-GFPHis. Assays were conducted 36 hours after transfection. Cells were washed three times with PBS (1 ml per well), before application of 0.5-ml assay buffer containing di-alanine with trace amounts of <sup>3</sup>H di-alanine. The buffer consisted of 120 mM NaCl, 2 mM MgSO<sub>4</sub>, and 20 mM Hepes (pH 7.5). After the desired time, the assay buffer was removed, and the cells were quickly washed twice with 0.5-ml assay buffer with no peptide. Cells were removed from the plate using trypsin, placed in a scintillation vial containing 100  $\mu$ l of 1 M NaOH, and lysed for 5 min before the addition of scintillation fluid. The amount of di-alanine taken up by the cells was calculated by scintillation counting in Ultima Gold (PerkinElmer) with comparison to a standard curve for the substrate. Experiments were performed for a minimal of four times to generate an overall mean and SD. To assess expression of the mutant variants within the cells, one well of each plate was harvested and lysed through freeze-thawing. Membranes were pelleted at 120,000g for 60 min, and the subsequent membrane pellet was solubilized in 20- $\mu$ l PBS containing 1% DDM:CHS. Ten microliters of each sample was loaded onto an 8% SDS-PAGE gel, and Western blot was performed using an anti-GFP antibody. The data shown in Fig. 4D are a percentage compared to WT of the amount transported after 6 min; “empty” refers to cells transfected with the empty plasmid, pLexM-GFP.

### Identification and screening of nanobodies

To identify PepT2-specific nanobodies, a library raised from immunization of a llama with reconstituted full length or ECD and screened using C-terminally biotinylated protein using a method modified from (51). Specifically, nanobodies were raised in a llama following intramuscular immunization with purified protein reconstituted into liposomes and using GERBU LQ 3000 as the adjuvant. Immunizations and handling of the llama were performed under the authority of the project license PPL 70/8108. Blood (150 ml) was collected, and peripheral blood mononuclear cells were prepared using Ficoll-Paque PLUS according to the manufacturers’ protocol. Total RNA was extracted using TRIzol and VHH cDNAs were generated by reverse transcription PCR using primer “CALL\_GSP” (table S1). The pool of VHH encoding sequences were amplified by two rounds of nested PCR: first with “CALL\_001” and “CALL\_002,” followed by “VHH\_For” and “VHH\_Rev\_IgG2” as well as “VHH\_Rev\_IgG3,” and cloned into the Sfi I sites of the phagemid vector pADL-23c. In this vector, the VHH encoding sequence is preceded by a pelB leader sequence followed by a linker, His6, and cMyc tag (GPGGQH-HHHGAEQKLISEEDLS). Electrocompetent *E. coli* TG1 cells were transformed with the recombinant pAD-23c vector resulting in a VHH library of about 2  $\times$  10<sup>8</sup> independent transformants. The resulting TG1 library stock was then infected with M13K07 helper phage to obtain a library of VHH-presenting phages. Phages displaying

VHs specific for PepT2-ECDA were enriched after two rounds of biopanning on 50 and 5 nM biotinylated PepT2-ECDA, respectively, through capturing with Dynabeads M-280 (Thermo Fisher Scientific). Enrichment after each round of panning was determined by plating the cell culture with 10-fold serial dilutions. After the second round of panning, 93 individual phagemid clones were picked; VHH displaying phages were recovered by infection with M13K07 helper phage and tested for binding to PepT2-ECDA by enzyme-linked immunosorbent assay (ELISA). Phage binders were ranked according to the ELISA signal and grouped according to CDR3 sequence identity.

ELISA-positive clones were sequenced, and unique nanobodies were identified as previously described (50). These were further characterized using biolayer interferometry using an Octet Red385 (Sartorius) and streptavidin biosensors loaded with biotinylated PepT2 at 100 nM in 20 mM Tris (pH 7.5), 150 mM NaCl, 0.03% DDM, and 0.006% CHS to compare  $k_{\text{on}}$  and  $k_{\text{off}}$ . To calculate  $K_{\text{d}}$ , a serial dilution of the nanobody from 500 to 3.9 nM was made, and following a 60-s baseline step, the nanobody was allowed to associate for 300 s followed by a dissociation step of 300 s. Data were analyzed in the Octet v9.0 software package and fit to a single binding site model in Prism. All raw data were baseline and reference subtracted, in-step corrected,  $y$ -axis aligned, and filtered with a Savitzky-Golay filter. The nanobodies exhibiting the slowest off rate were analyzed for coelution with PepT2 via size exclusion chromatography on a Superdex 200 column at pH 7.5 at 4°C.

### Cryo-EM sample preparation and data acquisition

Cryo-EM sample preparation, data acquisition, and processing were carried out as described in (50). PepT2 after size exclusion was mixed with a 1.2 M excess of nanobody D8 and incubated on ice for at least 30 min, and the complex was separated via size exclusion chromatography as above. PepT2-nanobody complex was concentrated to 4.2 mg/ml and adsorbed to glow-discharged holey carbon-coated grids (Quantifoil 300 mesh, Au R1.2/1.3) for 10 s. Grids were then blotted for 2 s at 100% humidity at 8°C and frozen in liquid ethane using a Vitrobot Mark IV (Thermo Fisher Scientific).

Data were collected in counted super-resolution mode on a Titan Krios G3 (FEI) operating at 300 kV with a BioQuantum imaging filter (Gatan) and K3 direct detection camera (Gatan) at  $\times 105,000$  magnification, with a physical pixel size of 0.832 Å. Initially, 21,739 movies were collected at a dose rate of 22.2  $e^{-}/\text{Å}^2$  per second, exposure time of 2.66 s, corresponding to a total dose of 59.1  $e^{-}/\text{Å}^2$  over 40 fractions. An additional 22,805 movies were collected at a dose rate of 21.4  $e^{-}/\text{Å}^2$  per second, exposure time of 2.66 s, corresponding to a total dose of 56.9  $e^{-}/\text{Å}^2$  over 40 fractions.

### Cryo-EM data processing

Movie processing was performed in real time using the SIMPLE pipeline (52), using SIMPLE-unblur for patched (15  $\times$  10) motion correction, SIMPLE-CTFFIND for patched contrast transfer function estimation, and SIMPLE-picker for particle picking. After initial 2D classification in SIMPLE to remove junk particles, all subsequent processing was performed in either cryoSPARC (53) or RELION-3.1 (54) using the `csparc2star.py` script within UCSF pyem (55) to convert between formats. Resolution estimates were derived from gold-standard Fourier shell correlations (FSCs) using the 0.143 criterion as calculated within RELION-3.1 (54), cryoSPARC (v2.15.0) (53), or the remote 3DFSC (56) processing server. Local resolution estimations were calculated within RELION-3.1 (54).

The cryo-EM processing workflow for PepT2 is outlined in fig. S3. Briefly, after 2D classification in SIMPLE using cluster2D-stream to remove junk particles, a model was generated ab initio in SIMPLE (52). This initial model was low-pass-filtered to 30 Å and used as reference for unsupervised 3D classification in RELION-3.1 (54) against 2,055,487 particles selected from the initial dataset. TM helices were apparent in only one class; particles (510,976) belonging to this class were subjected to 3D autorefinement in RELION resulting in a map of modest resolution (6.9 Å). This map was low-pass-filtered to 20 Å and used as reference for unsupervised 3D classification against 1,826,753 “cleaned” particles from the later dataset, generating a class with 338,477 particles that produced a moderate resolution map (7.1 Å) after 3D autorefinement in RELION-3.1. Refined particle subsets from both datasets were Bayesian polished in RELION-3.1, combined, and subjected to reference-free 2D classification ( $k = 200$ ) in cryoSPARC. cryoSPARC multiclass ab initio reconstruction from these particles (463,053) in cryoSPARC generated two volumes with strong TM helices and one “junk” volume.

Larger particle subsets from earlier within the processing pipeline were imported into cryoSPARC and subjected to two rounds of 2D classification ( $k = 200$  for each round) followed by heterogeneous refinement against the three ab initio maps, low-pass-filtered to 8 Å. Particles belonging to the two best classes were subjected to nonuniform refinements (57) against their corresponding 8 Å low-pass-filtered maps, generating volumes with global resolution estimates of 6.4 or 4.7 Å. While density for the TM helices and nanobody were consistent across both volumes, density for the second IgG domain within the ECD was stronger in the 4.7 Å map due to packing against the nanobody, resulting in a stabilized conformation. Particles belonging to the higher-resolution reconstruction (437,817) were imported into RELION-3.1 and Bayesian polished in a 320  $\times$  320 box followed by another round of multiclass heterogeneous refinement in cryoSPARC against the same 8 Å low-pass-filtered reference maps as previous. Particles (298,562) belonging to the strongest class were subjected to cryoSPARC nonuniform refinement, generating an improved 3.8 Å map. Map quality was further improved to 3.5 Å by local nonuniform refinement in cryoSPARC using prior orientations, an 8 Å of low-pass-filtered reference, and a soft mask encompassing only protein.

### Model building and refinement

Guided by docking of a generic nanobody and the ECD of *R. norvegicus* PepT2 (PDB 5A9H), the model of PepT2 (Table 1) was generated de novo from the globally sharpened 3.5 Å map following multiple rounds of manual building using Coot v.0.9 (58) and real-space refinement in PHENIX v.1.18.2-3874 (59) using secondary structure, rotamer, and Ramachandran restraints. PepT2 model was validated using MolProbity (60) within PHENIX. Figures were prepared using UCSF ChimeraX v.1.1 (61) and PyMOL v.2.4.0 (The PyMOL Molecular Graphics System, v.2.0; Schrödinger).

### Molecular docking and pose refinement by MD

The protein and the ligand were prepared with the `prepare_ligand4.py` and `prepare_receptor4.py` from MGLTools 1.5.6. Docking was performed with `smina` (62) using the AutoDock Vina scoring function (26). The `smina` search space was defined using the `autobox_ligand` option based on the location of the dipeptide AF from the superimposed bacterial POT homolog (PDB: 4d2c and 4d2d) (21). All nine generated binding poses generated by `smina` were used.

The protein was embedded into a 1-palmitoyl-2-oleoyl-*sn*-glycero-3-phosphocholine membrane using the coarse-grain (martini\_3.0.b.3.2) self-assembly protocol (63). The membrane was edited to a ratio of POPE:POPG = 3:1 and equilibrated for a further of 1  $\mu$ s. The resulting coordinates were then converted to an atomistic representation by cg2at (64), which was then energy-minimized and equilibrated in a constant number, volume and temperature (NVT) ensemble with V-rescale (65) at 310 K for 200 ps and then in a constant number, pressure and temperature (NPT) ensemble with the Berendsen barostat at 1 bar (66) and the Nosé-Hoover thermostat (67) at 310 K for 25 ns. The nine binding poses obtained from docking were superimposed onto the protein, solvated with TIP3P (68) water, and neutralized with NaCl to a concentration of 0.15 M.

For each ligand (alanine, AF, FA, AA, AAA, FAQ, and YYY), four repeats were run with 200-ps NVT and 1-ns NPT equilibration followed by 100-ns production runs with the Parrinello-Rahman barostat (69) at 1 bar. The resulting trajectory for each ligand is clustered with the GROMACS 2020 (70) single linkage clustering function, and the frame from the largest cluster with the smallest average root mean square deviation (RMSD) from all other structures of that cluster was selected as the representative binding pose. To assess binding stability of ligand binding, the RMSD of the ligand was computed with respect to both the representative frame of the largest cluster and the initial docking pose, while the trajectory was superimposed via the C $\alpha$  of the residues within 10 Å of the ligand.

We superimposed the binding pose of valacyclovir from PepT<sub>Sh</sub> (PDB: 6GZ9) and valganciclovir from DtpA (PDB: 6GS4) to rPepT2. For the binding pose from PepT<sub>Sh</sub>, three distance restraints were imposed between the oxygen from Glu<sup>622</sup>, Asn<sup>192</sup>, and Asn<sup>348</sup> to the nitrogen from the valine group of valacyclovir at 0.3 nm with a force constant of 1000 kJ/mol per nm<sup>2</sup>. Replica exchange with solute tempering (71) was used to enhance the sampling of ligand conformation at 310, 385, 475, 575, 676, 777, 878, and 979 K (72). The resulting trajectory at 310 K was then clustered with gmx (70) cluster in the same fashion as the di- and tripeptides. The representative frame of the largest cluster was then used for an extra 100 ns of unbiased simulation where RMSF calculations were used to assess stability.

### ECD motion analysis

The motion of the ECD was analyzed by concatenating all the trajectories from nine ligands, nine binding poses, and four repeats. The resulting trajectory was superimposed via the C $\alpha$  of the TMD (residue IDs 4-404 and 606-707), and the RMSF was computed for the C $\alpha$  of all residues. The RMSF of the ECD was also computed when the trajectory was superimposed via the C $\alpha$  of the ECD (residue ID 413-599). To perform PCA, the whole trajectory was superimposed via the C $\alpha$  of the TMD, and the covariance matrix was computed for the ECD with gmx covar. The eigenvalues and eigenvectors were computed on the basis of the covariance matrix and were done with gmx anaefg.

### ABFE calculation

To obtain the ABFE of the ligands in the protein, Boresch restraint (73)-based calculations described previously by us (74) were used. The MDRestraintsGenerator (<https://github.com/bigginlab/MDRestraintsGenerator>) was used for generating the restraint for each ligand. For each ligand, three repeats were run with 200 ps of NVT and 1 ns of NPT equilibration followed by 30 ns of production with replica exchange performed every 1000 steps. The results were analyzed using alchemical analysis (75).

### PMF calculation

To obtain the free energy of disengaging the N terminus or the C terminus from the binding pocket, umbrella sampling was used. Two collective variables (CVs) were defined as the distance between the N terminus (name: N) and Glu<sup>622</sup>:OE1 and between the C terminus (atom name: OC2) and Arg<sup>57</sup>:NH2. For the route of initial N-terminal disengagement followed by C-terminal disengagement, the C-terminal distance was kept constant at 0.3 nm at 1000 kJ/mol per nm<sup>2</sup>, while the N-terminal distance was restrained from 0.3 to 1.0 nm with a step of 0.05 nm at 1000 kJ/mol per nm<sup>2</sup>. This was followed by keeping the N-terminal distance at 1.0 nm, while the C-terminal distance was restrained from 0.3 to 1.0 nm with a step of 0.05 nm at 1000 kJ/mol per nm<sup>2</sup>. For the route of initial C-terminal disengagement followed by N-terminal disengagement, the N-terminal distance was fixed at 0.3 nm, while the C-terminal distance was changed from 0.3 to 1.0 nm, which was followed by fixing the C-terminal distance at 1.0 nm and moving the N-terminal distance from 0.3 to 1.0 nm. The initial frames were generated using steered MD, where the CV was moved gradually from 0.3 to 1.0 nm across the 100-ns simulation. The production run was performed for 100 ns with replica exchanged performed every 1000 steps preceded by 200 ps of NVT and 1 ns of NPT equilibration. The free energy landscape was recovered with WHAM (weighted histogram analysis method) (76). Three runs were performed, where the SD was derived. Analysis of hydrogen bonds was computed with MDAAnalysis (77, 78).

### SUPPLEMENTARY MATERIALS

Supplementary material for this article is available at <http://advances.sciencemag.org/cgi/content/full/7/35/eabh3355/DC1>

[View/request a protocol for this paper from Bio-protocol.](#)

### REFERENCES AND NOTES

1. D. M. Matthews, in *Protein Absorption: Development and Present State of the Subject* (Wiley-Liss, 1991), pp. 414.
2. Y. J. Fei, Y. Kanai, S. Nussberger, V. Ganapathy, F. H. Leibach, M. F. Romero, S. K. Singh, W. F. Boron, M. A. Hediger, Expression cloning of a mammalian proton-coupled oligopeptide transporter. *Nature* **368**, 563–566 (1994).
3. H. Daniel, I. Rubio-Aliaga, An update on renal peptide transporters. *Am. J. Physiol. Renal Physiol.* **284**, F885–F892 (2003).
4. M. Brandsch, I. Knütter, E. Bosse-Doenecke, Pharmaceutical and pharmacological importance of peptide transporters. *J. Pharm. Pharmacol.* **60**, 543–585 (2008).
5. K. Ito, A. Hikida, S. Kawai, V. T. T. Lan, T. Motoyama, S. Kitagawa, Y. Yoshikawa, R. Kato, Y. Kawarasaki, Analysing the substrate multispecificity of a proton-coupled oligopeptide transporter using a dipeptide library. *Nat. Commun.* **4**, 2502 (2013).
6. M. Brandsch, Drug transport via the intestinal peptide transporter PepT1. *Curr. Opin. Pharmacol.* **13**, 881–887 (2013).
7. M. E. Ganapathy, W. Huang, H. Wang, V. Ganapathy, F. H. Leibach, Valacyclovir: A substrate for the intestinal and renal peptide transporters PEPT1 and PEPT2. *Biochem. Biophys. Res. Commun.* **246**, 470–475 (1998).
8. M. Sugawara, W. Huang, Y. J. Fei, F. H. Leibach, V. Ganapathy, M. E. Ganapathy, Transport of valganciclovir, a ganciclovir prodrug, via peptide transporters PEPT1 and PEPT2. *J. Pharm. Sci.* **89**, 781–789 (2000).
9. C. Colas, P. M.-U. Ung, A. Schlessinger, SLC transporters: Structure, function, and drug discovery. *Med. Chem. Commun.* **7**, 1069–1081 (2016).
10. H. Daniel, B. Spanier, G. Kottra, D. Weitz, From bacteria to man: Archaic proton-dependent peptide transporters at work. *Physiology* **21**, 93–102 (2006).
11. H. Daniel, G. Kottra, The proton oligopeptide cotransporter family SLC15 in physiology and pharmacology. *Pflügers Arch.* **447**, 610–618 (2004).
12. S. Newstead, Recent advances in understanding proton coupled peptide transport via the POT family. *Curr. Opin. Struct. Biol.* **45**, 17–24 (2017).
13. J. H. Beale, J. L. Parker, F. Samsudin, A. L. Barrett, A. Senan, L. E. Bird, D. Scott, R. J. Owens, M. S. P. Sansom, S. J. Tucker, D. Meredith, P. W. Fowler, S. Newstead, Crystal structures of the extracellular domain from PepT1 and PepT2 provide novel insights into mammalian peptide transport. *Structure* **23**, 1889–1899 (2015).

14. X.-Z. Chen, T. Zhu, D. E. Smith, M. A. Hediger, Stoichiometry and kinetics of the high-affinity H<sup>+</sup>-coupled peptide transporter PepT2. *J. Biol. Chem.* **274**, 2773–2779 (1999).
15. J. Sun, J. R. Bankston, J. Payandeh, T. R. Hinds, W. N. Zagotta, N. Zheng, Crystal structure of the plant dual-affinity nitrate transporter NRT1.1. *Nature* **507**, 73–77 (2014).
16. J. L. Parker, S. Newstead, Molecular basis of nitrate uptake by the plant nitrate transporter NRT1.1. *Nature* **507**, 68–72 (2014).
17. C.-H. Ho, S.-H. Lin, H.-C. Hu, Y.-F. Tsay, CHL1 functions as a nitrate sensor in plants. *Cell* **138**, 1184–1194 (2009).
18. N. R. Hajizadeh, J. Pieprzyk, P. Skopintsev, A. Flayhan, D. I. Svergun, C. Löw, Probing the architecture of a multi-PDZ domain protein: Structure of PDZK1 in solution. *Structure* **26**, 1522–1533.e5 (2018).
19. R. Noshiro, N. Anzai, T. Sakata, H. Miyazaki, T. Terada, H. J. Shin, X. He, D. Miura, K. Inui, Y. Kanai, H. Endou, The PDZ domain protein PDZK1 interacts with human peptide transporter PEPT2 and enhances its transport activity. *Kidney Int.* **70**, 275–282 (2006).
20. J. L. Parker, C. Li, A. Brinth, Z. Wang, L. Vogele, N. Solcan, G. Ledderboge-Vucinic, J. M. J. Swanson, M. Caffrey, G. A. Voth, S. Newstead, Proton movement and coupling in the POT family of peptide transporters. *Proc. Natl. Acad. Sci. U.S.A.* **114**, 13182–13187 (2017).
21. A. L. Lyons, J. L. Parker, N. Solcan, A. Brinth, D. Li, S. T. A. Shah, M. Caffrey, S. Newstead, Structural basis for polyspecificity in the POT family of proton-coupled oligopeptide transporters. *EMBO Rep.* **15**, 886–893 (2014).
22. M. Martinez Molledo, E. M. Quistgaard, A. Flayhan, J. Pieprzyk, C. Löw, Multispecific substrate recognition in a proton-dependent oligopeptide transporter. *Structure* **26**, 467–476.e4 (2018).
23. D. E. Smith, B. Clemencon, M. A. Hediger, Proton-coupled oligopeptide transporter family SLC15: Physiological, pharmacological and pathological implications. *Mol. Aspects Med.* **34**, 323–336 (2013).
24. N. Solcan, J. Kwok, P. W. Fowler, A. D. Cameron, D. Drew, S. Iwata, S. Newstead, Alternating access mechanism in the POT family of oligopeptide transporters. *EMBO J.* **31**, 3411–3421 (2012).
25. D. Harder, J. Stolz, F. Casagrande, P. Obrdlík, D. Weitz, D. Fotiadis, H. Daniel, DtpB (YhiP) and DtpA (TppB, YdgR) are prototypical proton-dependent peptide transporters of *Escherichia coli*. *FEBS J.* **275**, 3290–3298 (2008).
26. O. Trott, A. J. Olson, AutoDock Vina: Improving the speed and accuracy of docking with a new scoring function, efficient optimization, and multithreading. *J. Comput. Chem.* **31**, 455–461 (2010).
27. N. G. Aduri, B. K. Prabhala, H. A. Ernst, F. S. Jørgensen, L. Olsen, O. Mirza, Salt bridge swapping in the EXXERFYXY motif of proton-coupled oligopeptide transporters. *J. Biol. Chem.* **290**, 29931–29940 (2015).
28. S. Newstead, D. Drew, A. D. Cameron, V. L. G. Postis, X. Xia, P. W. Fowler, J. C. Ingram, E. P. Carpenter, M. S. P. Sansom, M. J. McPherson, S. A. Baldwin, S. Iwata, Crystal structure of a prokaryotic homologue of the mammalian oligopeptide-proton symporters, PepT1 and PepT2. *EMBO J.* **30**, 417–426 (2011).
29. R. L. Stanfield, I. A. Wilson, Protein-peptide interactions. *Curr. Opin. Struct. Biol.* **5**, 103–113 (1995).
30. M. Brandsch, Transport of drugs by proton-coupled peptide transporters: Pearls and pitfalls. *Expert Opin. Drug Metab. Toxicol.* **5**, 887–905 (2009).
31. P. D. Bailey, C. A. Boyd, J. R. Bronk, I. D. Collier, D. Meredith, K. M. Morgan, C. S. Temple, How to make drugs orally active: A substrate template for peptide transporter PepT1. *Angew. Chem. Int. Ed.* **39**, 505–508 (2000).
32. J. Våbenø, T. Lejon, C. U. Nielsen, B. Steffansen, W. Chen, H. Ouyang, R. T. Borchardt, K. Luthman, Phe-Gly dipeptidomimetics designed for the di-/tripeptide transporters PEPT1 and PEPT2: Synthesis and biological investigations. *J. Med. Chem.* **47**, 1060–1069 (2004).
33. C. Colas, M. Masuda, K. Sugio, S. Miyauchi, Y. Hu, D. E. Smith, A. Schlessinger, Chemical modulation of the human oligopeptide transporter 1, hPepT1. *Mol. Pharm.* **14**, 4685–4693 (2017).
34. R. P.-A. Berntsson, M. K. Doeven, F. Fusetti, R. H. Duurkens, D. Sengupta, S.-J. Marrink, A.-M. W. H. Thunnissen, B. Poolman, D.-J. Slotboom, The structural basis for peptide selection by the transport receptor OppA. *EMBO J.* **28**, 1332–1340 (2009).
35. J. R. Tame, G. N. Murshudov, E. J. Dodson, T. K. Neil, G. G. Dodson, C. F. Higgins, A. J. Wilkinson, The structural basis of sequence-independent peptide binding by OppA protein. *Science* **264**, 1578–1581 (1994).
36. E. Lehnert, J. Mao, A. R. Mehdipour, G. Hummer, R. Abele, C. Glaubitz, R. Tampé, Antigenic peptide recognition on the human ABC transporter TAP resolved by DNP-enhanced solid-state NMR spectroscopy. *J. Am. Chem. Soc.* **138**, 13967–13974 (2016).
37. E. M. Quistgaard, C. Low, F. Guettou, P. Nordlund, Understanding transport by the major facilitator superfamily (MFS): Structures pave the way. *Nat. Rev. Mol. Cell Biol.* **17**, 123–132 (2016).
38. N. Yan, Structural biology of the major facilitator superfamily transporters. *Annu. Rev. Biophys.* **44**, 257–283 (2015).
39. P. W. Fowler, M. Orwick-Rydmark, S. Radestock, N. Solcan, P. M. Dijkman, J. A. Lyons, J. Kwok, M. Caffrey, A. Watts, L. R. Forrest, S. Newstead, Gating topology of the proton-coupled oligopeptide symporters. *Structure* **23**, 290–301 (2015).
40. J. L. Parker, J. A. Mindell, S. Newstead, Thermodynamic evidence for a dual transport mechanism in a POT peptide transporter. *eLife* **3**, e04273 (2014).
41. A. Steel, S. Nussberger, M. F. Romero, W. F. Boron, C. A. Boyd, M. A. Hediger, Stoichiometry and pH dependence of the rabbit proton-dependent oligopeptide transporter PepT1. *J. Physiol.* **498**, 563–569 (1997).
42. G. S. Minhas, S. Newstead, Structural basis for prodrug recognition by the SLC15 family of proton-coupled peptide transporters. *Proc. Natl. Acad. Sci. U.S.A.* **116**, 804–809 (2019).
43. Y. Ural-Blimke, A. Flayhan, J. Strauss, V. Rantos, K. Bartels, R. Nielsen, E. Pardon, J. Steyaert, J. Kosinski, E. M. Quistgaard, C. Löw, Structure of prototypic peptide transporter DtpA from *E. coli* in complex with valganciclovir provides insights into drug binding of human PepT1. *J. Am. Chem. Soc.* **141**, 2404–2412 (2019).
44. C. M. Perry, D. Faulds, Valaciclovir. A review of its antiviral activity, pharmacokinetic properties and therapeutic efficacy in herpesvirus infections. *Drugs* **52**, 754–772 (1996).
45. B. Yang, D. E. Smith, Significance of peptide transporter 1 in the intestinal permeability of valganciclovir in wild-type and PepT1 knockout mice. *Drug Metab. Dispos.* **41**, 608–614 (2013).
46. A. J. Eid, R. R. Razonable, New developments in the management of cytomegalovirus infection after solid organ transplantation. *Drugs* **70**, 965–981 (2010).
47. G. S. Minhas, S. Newstead, Recent advances in understanding prodrug transport through the SLC15 family of proton-coupled transporters. *Biochem. Soc. Trans.* **48**, 337–346 (2020).
48. M. Hauser, S. Kauffman, F. Naider, J. M. Becker, Substrate preference is altered by mutations in the fifth transmembrane domain of Ptp2p, the di/tri-peptide transporter of *Saccharomyces cerevisiae*. *Mol. Membr. Biol.* **22**, 215–227 (2005).
49. J. Elegheert, E. Behiels, B. Bishop, S. Scott, R. E. Woolley, S. C. Griffiths, E. F. X. Byrne, V. T. Chang, D. I. Stuart, E. Y. Jones, C. Siebold, A. R. Aricescu, Lentiviral transduction of mammalian cells for fast, scalable and high-level production of soluble and membrane proteins. *Nat. Protoc.* **13**, 2991–3017 (2018).
50. J. L. Parker, J. C. Deme, G. Kuteyi, Z. Wu, J. Huo, I. D. Goldman, R. J. Owens, P. C. Biggin, S. M. Lea, S. Newstead, Structural basis of antifolate recognition and transport by PCFT. *Nature* **595**, 130–134 (2021).
51. E. Pardon, T. Laeremans, S. Triest, S. G. F. Rasmussen, A. Wohlkönig, A. Ruf, S. Muyldermans, W. G. J. Hol, B. K. Kobilka, J. Steyaert, A general protocol for the generation of Nanobodies for structural biology. *Nat. Protoc.* **9**, 674–693 (2014).
52. J. Caesar, C. F. Reboul, C. Machello, S. Kiesewetter, M. L. Tang, J. C. Deme, S. Johnson, D. Elmlund, S. M. Lea, H. Elmlund, SIMPLE 3.0. Stream single-particle cryo-EM analysis in real time. *J. Struct. Biol. X* **4**, 100040 (2020).
53. A. Punjani, J. L. Rubinstein, D. J. Fleet, M. A. Brubaker, cryoSPARC: Algorithms for rapid unsupervised cryo-EM structure determination. *Nat. Methods* **14**, 290–296 (2017).
54. J. Zivanov, T. Nakane, S. H. W. Scheres, A Bayesian approach to beam-induced motion correction in cryo-EM single-particle analysis. *IUCr* **6**, 5–17 (2019).
55. D. Asarnow, E. Palovcak, Y. Cheng, UCSF pyem v0.5. Zenodo (2019).
56. Y. Z. Tan, P. R. Baldwin, J. H. Davis, J. R. Williamson, C. S. Potter, B. Carragher, D. Lyumkis, Addressing preferred specimen orientation in single-particle cryo-EM through tilting. *Nat. Methods* **14**, 793–796 (2017).
57. A. Punjani, H. Zhang, D. J. Fleet, Non-uniform refinement: Adaptive regularization improves single-particle cryo-EM reconstruction. *Nat. Methods* **17**, 1214–1221 (2020).
58. A. Brown, F. Long, R. A. Nicholls, J. Toots, P. Emsley, G. Murshudov, Tools for macromolecular model building and refinement into electron cryo-microscopy reconstructions. *Acta Crystallogr. D Biol. Crystallogr.* **71**, 136–153 (2015).
59. P. V. Afonine, B. K. Poon, R. J. Read, O. V. Sobolev, T. C. Terwilliger, A. Urzhumtsev, P. D. Adams, Real-space refinement in PHENIX for cryo-EM and crystallography. *Acta Crystallogr. D Struct. Biol.* **74**, 531–544 (2018).
60. M. G. Prisant, C. J. Williams, V. B. Chen, J. S. Richardson, D. C. Richardson, New tools in MolProbity validation: CaBLAM for CryoEM backbone, UnDowser to rethink “waters,” and NGL Viewer to recapture online 3D graphics. *Protein Sci.* **29**, 315–329 (2020).
61. E. F. Pettersen, T. D. Goddard, C. C. Huang, E. C. Meng, G. S. Couch, T. I. Croll, J. H. Morris, T. E. Ferrin, UCSF ChimeraX: Structure visualization for researchers, educators, and developers. *Protein Sci.* **30**, 70–82 (2021).
62. D. R. Koes, M. P. Baumgartner, C. J. Camacho, Lessons learned in empirical scoring with smina from the CSAR 2011 benchmarking exercise. *J. Chem. Inf. Model.* **53**, 1893–1904 (2013).
63. P. J. Stansfeld, J. E. Goose, M. Caffrey, E. P. Carpenter, J. L. Parker, S. Newstead, M. S. P. Sansom, MemProtMD: Automated insertion of membrane protein structures into explicit lipid membranes. *Structure* **23**, 1350–1361 (2015).
64. R. C. owen vickery, owenvickery/cg2at: CG2AT2 a fragment based conversion (Version v0.2) Zenodo (21 August 2020).

65. G. Bussi, D. Donadio, M. Parrinello, Canonical sampling through velocity rescaling. *J. Chem. Phys.* **126**, 014101 (2007).
66. H. J. Berendsen, J. P. M. Postma, W. F. van Gunsteren, A. DiNola, J. R. Haak, Molecular dynamics with coupling to an external bath. *J. Chem. Phys.* **81**, 3684–3690 (1984).
67. D. J. Evans, B. L. Holian, The Nose-Hoover thermostat. *J. Chem. Phys.* **83**, 4069–4074 (1985).
68. W. L. Jorgensen, J. Chandrasekhar, J. D. Madura, Comparison of simple potential functions for simulating liquid water. *J. Chem. Phys.* **79**, 926–935 (1983).
69. M. Parrinello, A. Rahman, Polymorphic transitions in single crystals: A new molecular dynamics method. *J. Appl. Phys.* **52**, 7182–7190 (1981).
70. M. J. Abraham, T. Murtola, R. Schulz, S. Páll, J. C. Smith, B. Hess, E. Lindahl, GROMACS: High performance molecular simulations through multi-level parallelism from laptops to supercomputers. *SoftwareX* **1-2**, 19–25 (2015).
71. P. Liu, B. Kim, R. A. Friesner, B. J. Berne, Replica exchange with solute tempering: A method for sampling biological systems in explicit water. *Proc. Natl. Acad. Sci. U.S.A.* **102**, 13749–13754 (2005).
72. A. Patriksson, D. van der Spoel, A temperature predictor for parallel tempering simulations. *Phys. Chem. Chem. Phys.* **10**, 2073–2077 (2008).
73. S. Boresch, F. Tettering, M. Leitgeb, M. Karplus, Absolute binding free energies: A quantitative approach for their calculation. *J. Phys. Chem. B* **107**, 9535–9551 (2003).
74. M. Aldeghi, A. Heifetz, M. J. Bodkin, S. Knapp, P. C. Biggin, Predictions of ligand selectivity from absolute binding free energy calculations. *J. Am. Chem. Soc.* **139**, 946–957 (2017).
75. P. V. Klimovich, M. R. Shirts, D. L. Mobley, Guidelines for the analysis of free energy calculations. *J. Comput. Aided Mol. Des.* **29**, 397–411 (2015).
76. A. Grossfield, WHAM: The weighted histogram analysis method, version 2.0.10.2.
77. N. Michaud-Agrawal, E. J. Denning, T. B. Woolf, O. Beckstein, MDAanalysis: A toolkit for the analysis of molecular dynamics simulations. *J. Comput. Chem.* **32**, 2319–2327 (2011).
78. P. Smith, R. M. Ziolk, E. Gazzarrini, D. M. Owen, C. D. Lorenz, On the interaction of hyaluronic acid with synovial fluid lipid membranes. *Phys. Chem. Chem. Phys.* **21**, 9845–9857 (2019).

**Acknowledgments:** We thank T. Sobajima for assistance with fluorescence microscopy.

**Funding:** The Central Oxford Structural Microscopy and Imaging Centre is supported by the Wellcome Trust (201536), The EPA Cephalosporin Trust, and a Royal Society/Wolfson Foundation Laboratory Refurbishment grant (WL160052). Computing was supported via the Advanced Research Computing facility, Oxford; the ARCHER UK National Supercomputing Service; and JADE (EP/T022205/1) granted via the High-End Computing Consortium for Biomolecular Simulation (HECBioSim; www.hecbiosim.ac.uk), supported by the EPSRC (EP/R029407/1). This research was supported by Wellcome Awards to S.M.L. (209194 and 100298), P.C.B. (219531), and S.N. (215519 and 219531) and through MRC grants to S.M.L. (MR/M011984/1) and J.L.P. (MR/S021043/1). Z.W. is a Wellcome Trust Ph.D. student (203741).

**Author contributions:** J.L.P. and S.N. conceived the project. G.K. maintained cell stocks and undertook large-scale expression and tissue culture. S.N. and J.L.P. performed all protein preparation. J.H. and R.J.O. generated and screened the llama library. J.C.D. and S.M.L. performed all cryo-EM sample processing, data collection, and image analysis. J.C.D., S.M.L., and S.N. constructed the atomic models. J.L.P. conducted all transport and biochemical assays. Z.W. and P.C.B. performed all MD analysis. J.L.P. and S.N. wrote the manuscript and prepared figures with contributions and discussions from Z.W., P.C.B., J.C.D., and S.M.L. **Competing interests:** The authors declare that they have no competing interests. **Data and materials availability:** Atomic coordinates for PepT2 have been deposited in the PDB under ID 7NQK and maps in Electron Microscopy Data Bank under ID 12528. The plasmids for expression of rat PepT2 and the nanobody have been deposited in Addgene under IDs 167988 and 167989. All data needed to evaluate the conclusions in the paper are present in the paper and/or the Supplementary Materials.

Submitted 3 March 2021

Accepted 2 July 2021

Published 25 August 2021

10.1126/sciadv.abh3355

**Citation:** J. L. Parker, J. C. Deme, Z. Wu, G. Kuteyi, J. Huo, R. J. Owens, P. C. Biggin, S. M. Lea, S. Newstead, Cryo-EM structure of PepT2 reveals structural basis for proton-coupled peptide and prodrug transport in mammals. *Sci. Adv.* **7**, eabh3355 (2021).